MDA5-mediated type I interferonopathy mouse model displays lethal response to immune stimulation

EMRALINO, Francine Lianne Castaneda

Table of Contents

Abstract 4

Abbreviations 5

Chapter 1: INTRODUCTION 7

1.1 RIG-I like receptors 8

1.2 Autoimmune disease and hypercytokinemia 10

1.3 Type I interferonopathies 11

1.4 Gender differences 12

1.5 Disease mechanism of SMS 12

1.6 Mouse models of SMS 14

Chapter 2: MATERIALS AND METHODS 15

2.1 Mice 16

2.2 Treatments and infection 16

2.3 Histology and immunohistochemistry 17

2.4 RNA isolation and quantification 17

2.5 Biochemical tests 17

2.6 Enzyme-Linked Immunosorbent Assay 18

2.7 Cell Isolation and Flow cytometry 19

2.8 Bone phenotype analysis 20

2.9 In vitro differentiation of osteoclasts 20

2.10 Eye phenotype analysis 21

2.11 Statistics 21

Chapter 3: RESULTS 22

3.1 hM-R822Q Tg mice display spontaneous systemic inflammation 23

3.2 hM-R822Q Tg mice exhibited developmental and bone abnormalities 29

3.3 hM-R822Q Tg mice exhibited SMS-like cardiac pathogenesis 31

3.4 Poly(I:C) induced lethal inflammation in female C57BL/6J hM-R822Q Tg mice 33

3.5 hM-R822Q Tg response to poly(I:C) is determined by background 39

3.6 MAVS and IFNAR dependent inflammation and poly(I:C) induced pathology 41

3.7 JAK signaling is critical for organ damage and lethality of poly(I:C) treatment 43

Chapter 4: DISCUSSION 45

Chapter 5: REFERENCES 50

Chapter 6: ACKNOWLEDGEMENTS 58

Abstract

Melanoma differentiation-associated protein 5 (MDA5) is a viral dsRNA sensor that has been associated with the development of autoimmune interferonopathies, including Singleton-Merten Syndrome (SMS) and Aicardi-Goutières Syndrome (AGS). The c.2465G>A (p.R822Q) missense mutation in the MDA5 gene interferon induced with helicase C domain 1 (*IFIH1*) has been identified as a gain-of-function mutation leading to SMS. This study aims to understand how this mutation affects the mechanism of disease progression and how external factors such as infection or immune stimulation with vaccination can impact the immune response of affected individuals. Mice with human MDA5 bearing the R822Q mutation (hM-R822Q Tg mice) developed SMS-like bone abnormalities, heart fibrosis, aortic valve enlargement, and aortic calcification. In these mice, a systemic interferon-stimulated gene (ISG) signature leads to the activation of both the innate and adaptive immune response. Administration of the polyinosinic-polycytidylic acid (poly(I:C)), which mimics viral dsRNA, produced dramatic systemic inflammation, most notable in the intestines. Poly(I:C)-injected female C56BL/6J hM-R822Q Tg mice developed lethal hypercytokinemia marked by massive IL-6 levels in the serum. This lethality was not observed in male C56BL/6J, nor in BALB/c hM-R822Q Tg mice. MAVS or IFNAR1 knock out interrupted the interferon signal and ameliorated hyperinflammation in hMR822Q Tg mice. Poly(I:C)-induced cytokine production and mucosal damage were also reduced with the introduction of tofacitinib, which is an inhibitor of JAK signaling. These findings demonstrate that the MDA5 R822Q mutant introduces a critical risk factor for developing severe disease symptoms upon viral infection or vaccination. Furthermore, hM-R822Q Tg mice model the importance of factors such as gender and genetic background in disease prognosis.

Abbreviations

α-SMA	alpha-smooth muscle actin
AGS	Aicardi–Goutières syndrome
APC	antigen presenting cell
ATP	adenosine triphosphate
CARD	caspase activation and recruitment domain
CAVD	calcified aortic valve disease
CTD	C-terminal domain
DC	dendritic cell
DDX58	DExD/H-box helicase 58
FoxP3	Forkhead box P3
GAPDH	glyceraldehyde 3-phosphate dehydrogenase
HEL	helicase
hM-R822Q	human MDA5 with p.R822Q (*IFIH1* c.2465G>A) missense mutation
IAV	influenza A virus
IBD	inflammatory bowel disease
IFIH1	interferon induced with helicase C domain 1
Ifih1$^{gs/+}$ mice	mice harboring the single missense mutation G821S in *Ifih1*
IFN	interferon
IFN-I	type I interferon
IFNAR	interferon α/β receptor
IL	interleukin
IL6R	IL-6 receptor
i.p.	intraperitoneal
IRF	interferon regulatory factor
ISG	interferon-stimulated gene

JAK	Janus kinase
LGP2	laboratory of genetics and physiology 2
LPS	lipopolysaccharide
MAVS	mitochondrial antiviral signaling protein
M-CSF	macrophage colony-stimulating factor
MDA5	melanoma differentiation–association protein 5
NF-κB	nuclear factor kappa B
NK cell	natural killer cell
PAMP	pathogen-associated molecular pattern
Poly(I:C)	polyinosinic:polycytidylic acid; dsRNA synthetic analog
RA	rheumatoid arthritis
RANKL	receptor activator for NF-κB ligand
RIG-I	retinoic acid-inducible gene I
RLR	RIG-I–like receptor
RORγt	retinoic acid receptor-related orphan nuclear receptor
TLR	Toll-like receptor
SLE	Systemic Lupus Erythematosus
SMS	Singleton-Merten syndrome
STAT	signal transducer and activator of transcription
Th17	T helper 17
TNF	tumor necrosis factor
TRAP	tartrate-resistant acid phosphatase
Treg	regulatory T cell
WT	wild type

Chapter 1

INTRODUCTION

1.1 RIG-I like receptors

Melanoma Differentiation Associated gene 5 (MDA5), encoded by the interferon induced with helicase C domain 1 (*IFIH1*) gene, and Retinoic Acid Inducible Gene I (RIG-I), encoded by DExD/H-box helicase 58 gene (*DDX58*), belong to a family of cytosolic double-stranded RNA (dsRNA) receptors known as RIG-I-like receptors (RLRs). They recognize RNA features not physiologically common in the cytosol, including double-stranded, 5'-triphosphate, or diphosphate ends. Their ability to recognize RNA viruses, as well as RNA intermediates of DNA virus transcription, make RLRs key effectors in the antiviral response. A third RLR, Laboratory of Genetics and Physiology 2 (LGP2), acts as a regulator of RIG-I/MDA5-mediated activation. RIG-I and MDA5 are composed of amino-terminal tandem caspase activation and recruitment domains (CARDs), a central helicase domain (HEL), and a C-terminal domain (CTD). RIG-I or MDA5 CARDs, which are structurally exposed upon binding with compatible RNA ligands, mediate signal transduction by interacting with the CARD of the membrane-bound mitochondrial antiviral signaling (MAVS) adaptor. MAVS then signals through transcription regulators such as interferon (IFN) regulatory factor 3 (IRF-3) and nuclear factor κB (NF-κB) (1, 2). This leads to the production of pro-inflammatory responses, including the expression of IFN-β and inflammatory cytokines. Further downstream, IFN-β binds the IFNα/β receptor (IFNAR), inducing the transcriptional upregulation of IFN-stimulated genes (ISGs) (3) and further stimulation of inflammatory cytokine expression (Fig. 1). ISGs can mediate antiviral response through an expanse of mechanisms such as degradation of viral RNA and inhibition of viral translation, assembly, and egress (4, 5).

IFNα and IFNβ are classified as type I interferons (IFN-I). IFN-I plays an important, though not well-elucidated, role in T cell activation (6). In general, activation of antigen presenting cells (APCs) such as dendritic cells (DCs), and natural killer cells (NKs), influence T cell maturation. One major signaling pathway induced by IFNs is the Janus kinase/signal transducer and activator of transcription (JAK/STAT) pathway. This promotes the production of antibodies and interleukins (ILs) such as IL-6 production, which, in turn, triggers the expression of retinoic acid

receptor-related orphan nuclear receptor (RORγt) and promotes T helper 17 (Th17) cell proliferation (7). JAK/STAT signaling also triggers a positive feedback loop which further increases RIG-I/MDA5 expression and activation and IFN-I production (8, 9).

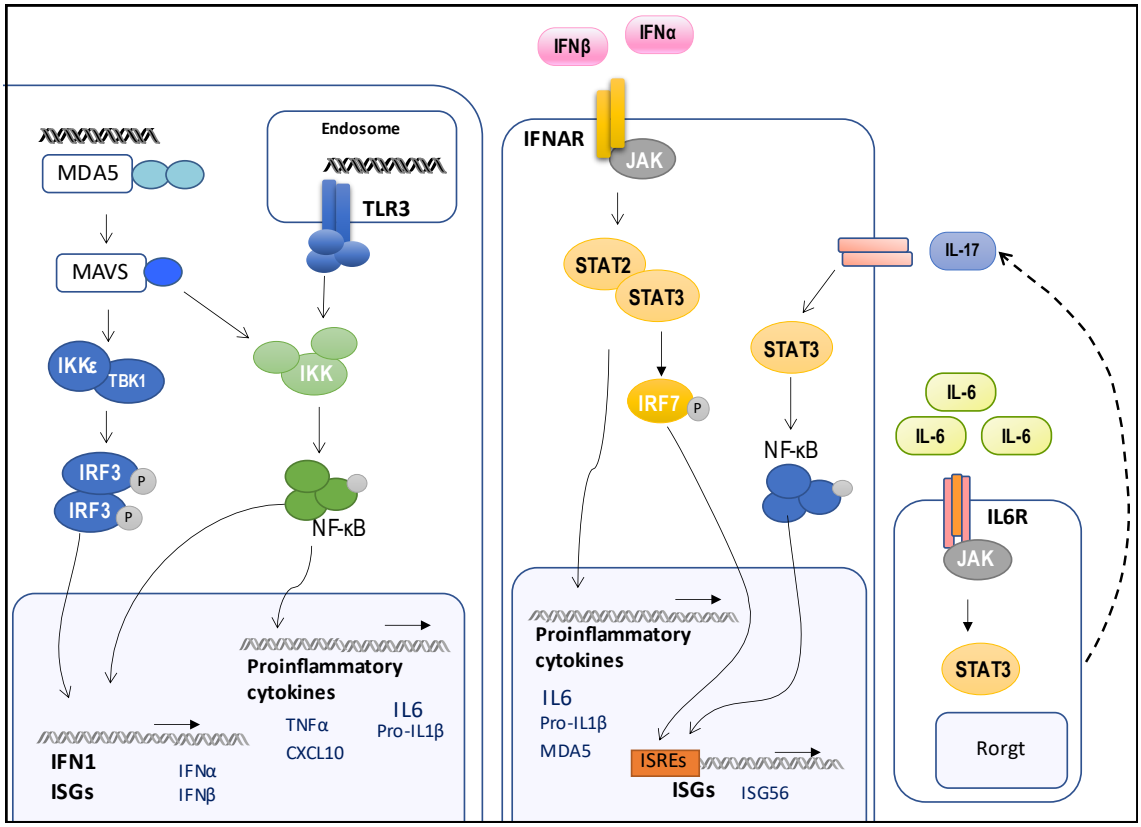

Figure 1. Activation of viral dsRNA sensors. Long dsRNAs are recognized by MDA5 in the cytosol and TLR3 through endosomes. MDA5 activates MAVS on the outer membrane of the mitochondria. This triggers a cascade of molecules that leads to the phosphorylation-mediated activation of several transcription factors including IRF3, IRF7, and NF-κB. IRF3 controls the expression of IFN-I, while NF-κB regulates the production of inflammatory cytokines. TLR3 similarly signals through IKK to activate NF-κB, promoting inflammatory cytokine production. Type 1 interferons IFNα and IFNβ signal through the IFNAR to activate the JAK/STAT signaling pathway, leading to both proinflammatory cytokine production and IRF7 translocation to the nucleus to bind to interferon-stimulated response elements (ISREs). Inflammatory cytokine IL-6 signals through the IL-6 receptor (IL6R) on T cells, inducing Rorγt expression in the nucleus through the JAK/STAT pathway, promoting Th17 differentiation.

1.2 Autoimmune disease and hypercytokinemia

The immune response to viruses relies on the sophisticated balance and coordinated function of several cell types and cytokines, encompassing both the innate and adaptive arms of the immune system. This vigorous response is crucial for viral clearance. Likewise, the resolution of the resulting inflammatory response is necessary, without which a potential for developing immunologically mediated disorder arises.

Systemic autoimmune diseases can be characterized as deregulation of the immune system, resulting in an individual's immune system attacking the body's own tissues. Patients of autoinflammatory disorders often have increased levels of proinflammatory cytokines, leading to inflammation, degeneration, tissue destruction, and even organ failure (10). Autoimmune diseases have been shown to result from both genetics and epigenetic modifications, including CpG-DNA methylation, histone modifications, and microRNAs (11).

Cytokine storm syndrome is characterized by elevated levels of circulating cytokines and immune cell hyperactivation. It represents a group of disorders resulting from sharing the outcome of overwhelming inflammation, macrophage activation, hemophagocytosis, and organ dysfunction, that may potentially lead to death. The response is often triggered by severe infection, although it may also occur in the absence of pathogens in cases of autoinflammatory disorders. A key component in cytokine storm is the failure of negative feedback mechanisms, including anti-inflammatory responses through regulatory cells and anti-inflammatory cytokines such as IL-10 that antagonize inflammatory cell populations and prevent hyperinflammation (12).

Among the involved cytokines, IL-6 seems to play a dominant role in cases of cytokine storm. High levels of IL-6 can activate the coagulation pathway and vascular endothelial cells and inhibit myocardial function. IL-6, as well as IL-1β, have also been associated with lower cytolytic functions of NK cells and $CD8^+$ T cells, leading to the inability to lyse infected cells for viral clearance, or active antigen presenting cells to resolve inflammation. High serum concentrations of IL-6 have been identified as markers of acute pancreatitis, rheumatoid arthritis (RA), Castleman disease, juvenile idiopathic arthritis, Crohn's disease, and severe symptomatology and

lethality infections such as SARS-CoV2 (13–15). Meanwhile, treatment through JAK inhibition and IL-6 blockade have been found to lower disease severity (16, 17).

1.3 Type I interferonopathies

A specific group of autoimmune disorders, interferonopathies are a heterogeneous group of disorders, mainly presenting an autosomal recessive inheritance pattern, characterized by constitutive upregulation of IFN-I. Early evidence linking IFN-I to autoimmunity was identified in patients receiving immunotherapy with IFNs for chronic viral infections or malignant carcinoid tumors (18). The autoantibodies and IFN signature observed in these patients were later found comparable to those presenting clinical manifestations of diseases such as systemic lupus erythematosus (SLE) and RA. Aicardi–Goutières syndrome (AGS), the most well-studied interferonopathy, is defined as an early onset progressive brain disease with occurrences of skin lesions referred to as chilblains, glaucoma, with symptoms resembling those of SLE (19). Mutations in different genes found to be associated with nucleotide metabolism and sensing, including TREX1, RNASEH2A, RNASEH2C, and ADAR1, have been correlated with different clinical manifestations of AGS, all of which present with IFN signature in the peripheral blood (20). These gave insight into the variety of mechanisms through which dysregulation of type I IFN signaling can occur. This includes uncontrolled activation of viral sensors through gain-of-function mutations or accumulation of endogenous pathogen-associated molecular patterns (PAMPs) through the dysfunction of enzymes responsible for nucleic acid degradation. Alterations in the function of signal regulators such as gain-of-function mutations of positive IFN signaling regulators and loss-of-function mutations of negative IFN signaling regulators similarly lead to constitutive activation of the IFN pathway (21). Positive IFN signaling may also be sustained by the loss of function of proteasomes that are meant to degrade these activator molecules (22).

Several studies have associated polymorphisms in the genes encoding RIG-I like receptors with autoimmune diseases such as multiple sclerosis, diabetes mellitus type 1, psoriatic arthritis, cutaneous psoriasis, and dermatomyositis (23–26). With the discovery of lupus-like nephritis and systemic autoimmune symptoms in MDA5 mutant mice, Funabiki et al. (27) solidified the link between RLR signaling and disease-causing immune dysregulation. More recently several groups identified gain-of-function mutations in RIG-I and MDA5 to be causative of Singleton-Merten Syndrome (SMS), SLE, or Aicardi-Goutières Syndrome (AGS) (19, 28–30).

1.4 Gender differences

Gender differences have been found to impact disease progression, symptoms, response to therapy, and clinical outcome. These manifestations are even more evident in the case of autoimmune diseases. A strong gender bias has been established towards females for a number of autoimmune diseases, including SLE and Sjögren's syndrome (31–33). This is coupled with a stronger immune response and antibody production in women during infection and vaccination (34–36). In contrast, a few immunological diseases such as ankylosing spondylitis, are more prevalent in males (37). Most studies have attributed this enhanced immune response to X-linked factors and hormones, such as estrogen, and even gut microbiota (38–40). Overall, the female immune system has a higher reactivity with an enhanced ability to produce antibodies and a stronger ability to mount an IFN-I response. Monocytes in females also display an increased antigen presenting activity (41). Meanwhile, males have increased numbers of regulatory T cells (Tregs) and are generally more susceptible to infections (41). No direct reports of sex differences in SMS have been made.

1.5 Disease mechanism of SMS

SMS is an autosomal dominant disease that presents primarily as skeletal, dental, and vascular abnormalities (42, 43). Calcifications of the aorta, aortic valve, and mitral valve in

childhood have been widely observed in SMS cases (44, 45). Most cases of death due to SMS have been attributed to the sequelae of calcifications and sudden death in patients is linked to the possibility of cardiac rhythm disturbance (28). Less common features include generalized muscle weakness, psoriasis, early-onset glaucoma, as well as recurrent infections (28, 30). SMS has been associated with mutations in *IFIH1*, which encodes MDA5, and *DDX58*, encoding RIG-I.

Whole-exome sequencing of DNA from families of SMS patients allowed the identification of a c.2465G>A (p.R822Q) missense mutation in *IFIH1* within the region that encodes the HEL2 helicase domain of MDA5, close to the ATP binding site. This mutation potentially alters the stability of MDA5 binding to nucleic acids, leading to sustained MDA5 activation. Overexpressing R822Q MDA5 in HEK293T cells resulted in MDA5 hyperactivity when challenged with a dsRNA analog, poly(I:C) (44). RIG-I mutations c.1118A>C (p.E373A) and c.803G>T (p.C268F) have also been shown to cause atypical SMS wherein patients exhibited variable symptoms without dental abnormalities (29). RIG-I SMS variants C268F and E373A are located within the ATP binding motifs and were shown to be constitutively active in reporter cells in the absence of an external dsRNA trigger (29) Impaired ATP hydrolysis in RIG-I E373A stabilizes non-specific binding of RIG-I to endogenous RNA. In contrast, RIG-I E373A binds dsRNA independent of ATP binding (46).

Sustained MDA5 or RIG-I signaling in SMS patients is believed to be due to self-RNA recognition (47). The constant interferon signal induced by these activated RIG-I like receptors leads to chronic inflammation that can lead to aberrant vascular calcification (48). In contrast, the same chronic inflammation can cause demineralization of hard tissues such as bones. Dysregulated RANKL expression induced by IFN-Is also leads to aberrant osteoclastogenesis (49).

1.6 Mouse models of SMS

In mice, N-ethyl-N-nitrosourea (ENU)-induced p.Glu821Ser substitution in *Ifih1* leads to chronic activation of MDA5. *Ifih1*$^{gs/+}$ mice develop lupus-like, SMS-like, and some AGS-linked symptoms, including nephritis, dermatitis, abnormal bone development, and encephalitis (27, 50, 51). These mice had upregulated expression of IFN-inducible genes and inflammatory cytokines. On the other hand, mice with human RIG-I E373A developed psoriatic skin lesions. In these mice, long-term inhibition of JAK1 and JAK3 signaling promoted healing, and pre-treatment from an early age prevented lesion development. In addition, IL-17A-deficient hRIG-I E373A Tg mice did not develop skin lesions, linking Th17 cells and the psoriasis phenotype (52). These observations underscore the notion that RLR signaling impacts numerous cell types. The effects of RLR dysregulation are thus expansive, leading to a plethora of disease symptoms. Consequently, effective treatment is heavily reliant on a better understanding of RLR dysregulation and the underlying mechanism.

Despite the availability of genetic data, differences in clinical symptoms in patients with similar gain-of-function mutations expose gaps in our knowledge of the development of interferonopathies. In order to closely examine the specific effects of the SMS-associated MDA5 mutation in vivo, a human MDA5 R822Q mutant transgene was introduced into mice. Inflammation-induced disease phenotype was monitored in these mice. Additionally, poly(I:C), which is known to induce signaling through MDA5 and toll-like receptor 3 (TLR3) (53, 54), was introduced to mimic active inflammation triggered by infection. This study demonstrated that, although the autoimmune activity at the basal level appears non-pathogenic, it pre-disposed hMDA5 R822Q Tg mice to a severe inflammatory response upon immune stimulation. I propose that hM-R822Q Tg mice are an effective model demonstrating SMS-like disease development and may be instrumental to the discovery of preventive and therapeutic treatments for both SMS-related spontaneous and induced disease.

Chapter 2

MATERIALS AND METHODS

2.1 Mice

A fragment of the human chromosome encompassing the *IFIH1* gene, together with its inherent promoter, was cloned using bacterial artificial chromosome (BAC) technology. This *IFIH1* gene was mutated to encode R822Q MDA5 and transferred by random insertion into C57BL/6J mice (Institute of Immunology Co. Ltd., Tokyo, Japan). Genotyping of hM-R822Q transgenic mice was performed through PCR amplification targeting exon 5 of the human *IFIH1* gene, including the site of the c.2465G>A missense mutation (forward primer 5' - TTCAGGCTTCCTAAGCTCG - 3'; reverse primer 5' - GAGTCAATGACACAAATGCC -3'). One line was confirmed to show germline transmission and all hM-R822Q Tg mice used in these experiments originated from that line and were heterozygous for the human MDA5 mutation. hM-R822Q Tg mice were crossed with *Ifnar1*$^{-/-}$ mice, purchased from B&K Universal, or *Mavs*$^{-/-}$ mice, gifted by S. Akira (Osaka University), to generate *Ifnar1*$^{-/-}$ and *Mavs*$^{-/-}$ hM-R822Q mice. BALB/c hM-R822Q Tg mice were generated by backcrossing C57BL/6J mice with wild-type (WT) BALB/c mice to the fifth cross. Mice were analyzed at 8-12 weeks of age unless otherwise specified. All mice were housed in a specific pathogen-free (SPF) facility.

2.2 Treatments and infection

Intraperitoneal (*i.p.*) injection of poly(I:C) (GE Healthcare) was done at 15 μg per gram body weight, diluted to 500 μL with phosphate-buffered saline (PBS) per mouse. LPS-EB (*E. coli* O111:B4) (Invivogen) was injected *i.p.* in 300 μL volumes at 1 μg per gram body weight. CP 690550 citrate (tofacitinib) (TOCRIS bioscience) was dissolved in a solution of 0.5% methylcellulose (Wako) /0.025% Tween 20 (Nacalai Tesque). Mice were administered with the tofacitinib solution at 0.03 mg/g given at 200 μL per mouse through oral gavage. All poly(I:C) injection and tofacitinib treatment experiments were performed on female mice unless otherwise specified.

Mice were anesthetized with pentobarbital through *i.p.* injection before intranasal administration of 30 μl of influenza A virus (IAV) (PR/8) at 100 PFU per 25 g of mouse.

2.3 Histology and immunohistochemistry

Tissue samples fixed in 4% paraformaldehyde phosphate (Nacalai Tesque) were embedded in paraffin. Hematoxylin and eosin (Sakura) were performed on 5 μm tissue sections. Picrosirius red staining was performed on heart and liver sections (5 μm) using Direct Red 80 (Sigma-Aldrich) in saturated picric acid solution and counterstained with hematoxylin. Stained sections were observed under a BZ-8000 microscope (KEYENCE). Immunofluorescence staining was performed on 2 μm sections and images were captured with a confocal microscope (Leica, TCS SP8). Histological analysis of tissues was performed through blind evaluation. Villous lifting, villous shortening, epithelial shedding, and cellular infiltration (localized or extensive) were used as criteria for numerical scoring of the intestines.

2.4 RNA isolation and quantification

Organ samples were homogenized for total RNA extraction using the TRIzol reagent (Invitrogen, Life Technologies) and transcribed using ReverTra Ace® qPCR RT Master Mix with gDNA Remover (TOYOBO). Real-time PCR was performed with Thunderbird SYBR qPCR mix (TOYOBO) on a StepOnePlus Real-Time PCR system (Applied Biosystems) using primers listed in Table 2. The expression of target genes was normalized to an endogenous reference, glyceraldehyde 3-phosphate dehydrogenase (GAPDH).

2.5 Biochemical tests

Aortic calcium was measured with a Colorimetric Calcium Detection Assay Kit (abcam) following the manufacturer's instructions. Briefly, aortas were collected and washed in cold PBS. Tissues were suspended in Calcium Assay Buffer and homogenized using a sonicator. After centrifugation, 50 μL of the sample supernatant was mixed with 90 μL of Chromogenic agent and 60 μL Calcium Assay Buffer. After 5-10 mins, the absorbance at 575 nm of each sample solution was read.

Table 1. qPCR primers

Gene		Sequence (Forward)	Sequence (Reverse)
Mouse	*Gapdh*	5′-CCCCAGCAAGGACACTGAGCAAG-3′	5′-GGGGTCTGGGATGGAAATTGTGAGG-3′
	Mda5	5′-GCTGCTAAAGACGGAAATCG-3′	5′-TCTTGTCGCTGTCATTGAGG-3′
	Ifnb	5′-GGTCCGAGCAGAGATCTTCA-3′	5′-CACTACCAGTCCCAGAGTCC-3′
	Ifng	5′-CTGAGACAATGAACGCTACACA-3′	5′-TTTCTTCCACATCTATGCCACT-3′
	Il1b	5′-CATCCAGCTTCAAATCTCGCAG-3′	5′-CACACACCAGCAGGTTATCATC-3′
	Il6	5′-CATGTTCTCTGGGAAATCGTGG-3′	5′-GTACTCCAGGTAGCTATGGTAC-3′
	Il10	5′-GCGTCGTGATTAGCGATGATG-3′	5′-CTCGAGCAAGTCTTTCAGTCC-3′
	Cxcl10	5′-CCATTCTGATTTGCTGCCTTA-3′	5′-GGCTTGCAGGAATAATTTCAA-3
	Isg56	5′-ATGGGAGAGAATGCTGATGG-3′	5′-CCCAATGGGTTCTTGATGTC-3′
	Tgfb	5′-GGAGAGCCCTGGATACCAAC-3′	5′-CAACCCAGGTCCTTCCTAAA-3′
	Tnfa	5′-GGCATGGATCTCAAAGACAACC-3′	5′-CAGGTATATGGGCTCATACCAG-3′
Human	*MDA5*	5′-GTCTGGGGCATGGAGAATAA-3′	5′-TGCCCATGTTGCTGTTATG-3′

2.6 Enzyme-Linked Immunosorbent Assay

Plasma IL-6 levels were measured using an ELISA MAX Deluxe Set Mouse IL-6 kit (BioLegend) using the manufacturer's instructions. Briefly, uncoated flat-bottom 96-well plates were coated with IL-6 capture antibody overnight at 4°C. Wells were washed before blocking for 1 hour at room temperature. After washing, samples were added to the wells and incubated at room temperature for 2 hours. The wells were washed again, and the Detection Antibody solution (100 µL) was added to the wells and incubated for another hour at room temperature. After washing, 100 µL Avidin-HRP solution was added to each well. After 30 mins at room temperature, the wells were washed carefully. The TMB Substrate solution (100 µL) was added to the wells and kept in the dark for 20 mins before the addition of stop solution. Absorbance was read at 450 nm with wavelength correction at 570 nm.

2.7 Cell Isolation and Flow cytometry

Spleens and Peyer's patches were harvested and cellularized by mechanical dissociation through a 70-µm filter. Splenocytes were treated with ammonium-chloride-potassium (AKT) lysis buffer. Surface antigens were stained with fluorochrome-conjugated antibodies (Table 2).

Table 2. Antibodies used for flow cytometry

Target		**Fluorochrome**	**Company**	**Catalog #**
mouse	CD3ε	PE	BioLegend	100308
mouse	CD4	Pe/cyanine7	BioLegend	100528
mouse	CD8a	PerCP	BioLegend	100732
mouse	CD11b	PE	BioLegend	101208
mouse	CD11c	PE	BioLegend	117308
mouse	CD19	APC	BioLegend	115512
mouse	CD44	Alexa Fluor 488	BioLegend	103016
mouse	CD45R/B220	APC	Pharmigen, BD	553092
mouse	CD62L	PE	Pharmigen, BD	561918
mouse	CD69	Alexa Fluor 488	BioLegend	104516
mouse	CD86	Alexa Fluor 488	BioLegend	105108
mouse	F4/80	APC	BioLegend	123116
mouse	FoxP3	APC	eBioscience	17-4776-41
mouse	IFNγ	PE	BioLegend	505807
mouse	IL-6	APC	BioLegend	504507
mouse	NK1.1	APC	BioLegend	108709
mouse	Rorγt	PE	Pharmigen, BD	562607

Dendritic cells were stained after $CD19^+$ and $CD3\varepsilon^+$ cell depletion using MACS cell separation (Miltenyi Biotech). For the detection of IL-17a, IL-6, and IFN-γ staining, cells were first stimulated with PMA/ionomycin (Sigma-Aldrich) for 4-5 hours at 37°C, with the addition of monensin (1:1000) after 1 hour of incubation. Intracellular markers were stained using a FoxP3

Fixation/Permeabilization kit (eBioscience). Fluorescence-activated cell sorting (FACS) was performed using a BD LSRFortessa X-20 (BD Biosciences) system. Data were analyzed with the FlowJo software (Tomy Digital Biology).

2.8 Bone phenotype analysis

Femurs of 14-week-old female mice fixed in 70% ethanol were subjected to microcomputed tomography (μCT) and scanned using a ScanXmate-L090H (Comscantecno) system as described by Kurotaki, et. al (55). The coneCTexpress (WhiteRabbit) and TRI/3DBON-FCS (RATOC Systems) systems were used for the reconstruction and analysis of the three-dimensional microstructural image data. These femoral bones and bone mineral density analyses were performed by Dr. N. Sakai and M. Takami at Showa University in Tokyo.

2.9 In vitro differentiation of osteoclasts

Bone marrow cells were obtained by flushing the femurs and tibiae of mice with α-MEM (Nacalai Tesque). Cells were suspended in α-MEM containing a combination of 100 U/ml penicillin and 100 mg/ml streptomycin (Nacalai Tesque), and 10% FBS (Life Technologies), supplemented with 10 ng/ml M-CSF (R&D Systems). Cultures were rinsed with PBS after 3 days. Attached bone-marrow-derived macrophages (BMMs) were collected by treatment with trypsin-EDTA (2.5g-1mMol, Nacalai Tesque). BMMs were cultured in a medium containing 10 ng/ml of macrophage colony-stimulating factor (M-CSF) (R&D Systems) and 40 ng/ml of receptor activator of NF-kB ligand (RANKL) (R&D Systems) for 4 days, with medium change on the second day. Differentiated osteoclasts were fixed with 4% paraformaldehyde and stained using a telomerase repeat amplification protocol (TRAP). TRAP activity was measured in cell lysates using a TRAP & alkaline phosphatase (ALP) assay (Takara Bio) as a means of quantifying osteoclast differentiation.

2.10 Eye phenotype analysis

Mice were anesthetized through intramuscular injection of a ketamine (70 mg/kg)/xylazine (14 mg/kg) mixture. intramuscular injection of a ketamine (70 mg/kg)/xylazine (14 mg/kg) mixture. Mice were injected with 10% sodium fluorescein dye (10 ml/kg). Mouse corneas were treated with hydroxyethyl cellulose eye solution and fitted with a polymethyl methacrylate contact lens to prevent corneal drying. Spectral domain optical coherence tomography (SD-OCT) was performed using a customized Multiline OCT (Heidelberg Engineering) based on the settings described by Hasegawa, et al. (56). SD-OCT was performed by Dr. H. Ikeda of Kyoto University Hospital.

2.11 Statistics

Statistical analyses were performed using GraphPad Prism, version 9.0 (GraphPad Software, San Diego, CA, USA). Differences between 2 experimental groups were analyzed using a two-tailed *t*-test. Multiple comparisons were performed using a one-way analysis of variance (ANOVA) test. A value of $p < 0.05$ was considered statistically significant (*$p \leq 0.05$, **$p \leq 0.01$, ***$p \leq 0.001$, *** $p \leq 0.0001$).

Chapter 3

RESULTS

3.1 hM-R822Q Tg mice display spontaneous systemic inflammation

The variety of diseases induced by gain-of-function mutations on MDA5 highlights our limited understanding of the role of RIG-I like receptors in vivo. To gain a better understanding of the role of R822Q MDA5 in SMS, transgenic mice were generated through the insertion of a BAC carrying the mutated genomic human MDA5 into the genome of C57BL/6J and BALB/c mice. *IFIH1* mRNA expression was confirmed in various organs of hM-R822Q Tg mice (Fig. 1A). Mouse *Ifih1* was also found to be highly upregulated in hM-R822Q Tg mice when compared with WT expression (Fig. 1B). This corresponded to very strong expression of human and mouse MDA5, notably elevated in comparison to WT and comparable to immune-stimulated WT mice (Fig. 1C).

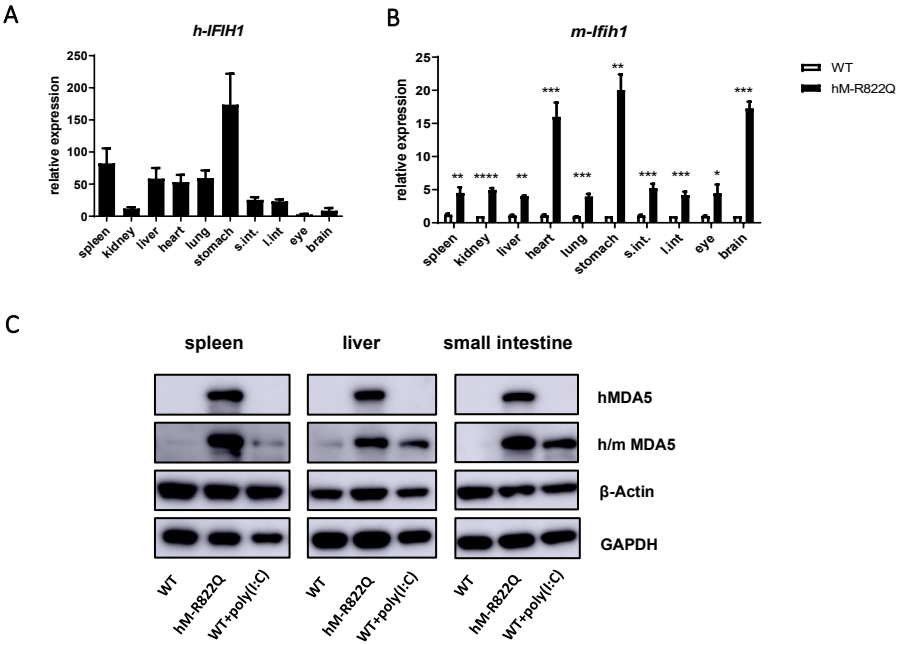

Figure 2. MDA5 expression in hM-R822Q Tg mice. The mRNA expression of human MDA5 *IFIH1* (A) and mouse MDA5 *Ifih1* (B) were tested on multiple organs of 8-10 week old mice (n=3). (C) Protein expression was evaluated with a monoclonal antibody specific for hMDA5 and a polyclonal antibody recognizing both human and mouse MDA5. Graphs are presented as mean ± SEM. Statistical significance was determined using Student's *t*-test (**p*<0.05, ***p*<0.01, ****p*<0.001)

In *Ifih1*$^{gs/+}$ mice, 60% mortality was observed within 24 weeks after birth (27). Both male and female hM-R822Q mice lived an average of 80 weeks (Fig. 3) without any clear evidence of fatal disease. Co-housed WT mice lived for over 140 weeks in the same SPF conditions. To gain insight into this, inflammation and inflammation-induced damage were assessed in various organs. Initial observation of internal organs revealed visible signs of lymph node inflammation (Fig. 4A), liver discoloration (Fig. 4B), and splenomegaly (Fig. 4C). All investigated organs in hM-R822Q Tg mice showed upregulation of inflammatory cytokines and ISGs such as *Ifnb*, *Isg56*, *Il1b*, *Tnfa*, and *Il6* (Fig. 4D). IFN levels were particularly elevated in mucosal regions, such as the intestines, lungs, and eyes. In contrast, the levels of cytokines more commonly associated with the regulation of inflammation, such as *Tgfb* and *Il10*, did not significantly differ between the Tg and WT mice in all organs tested (Fig. 4E).

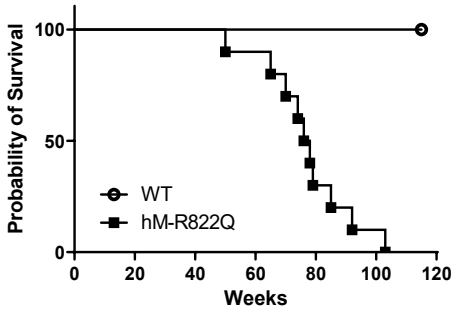

Figure 3. hM-R822Q Tg mice display shortened lifespans. Survival graph of WT and hM-R822Q Tg mice monitored for 150 weeks. Statistical significance was determined using the Kaplan-Meier estimate (**p<0.01).

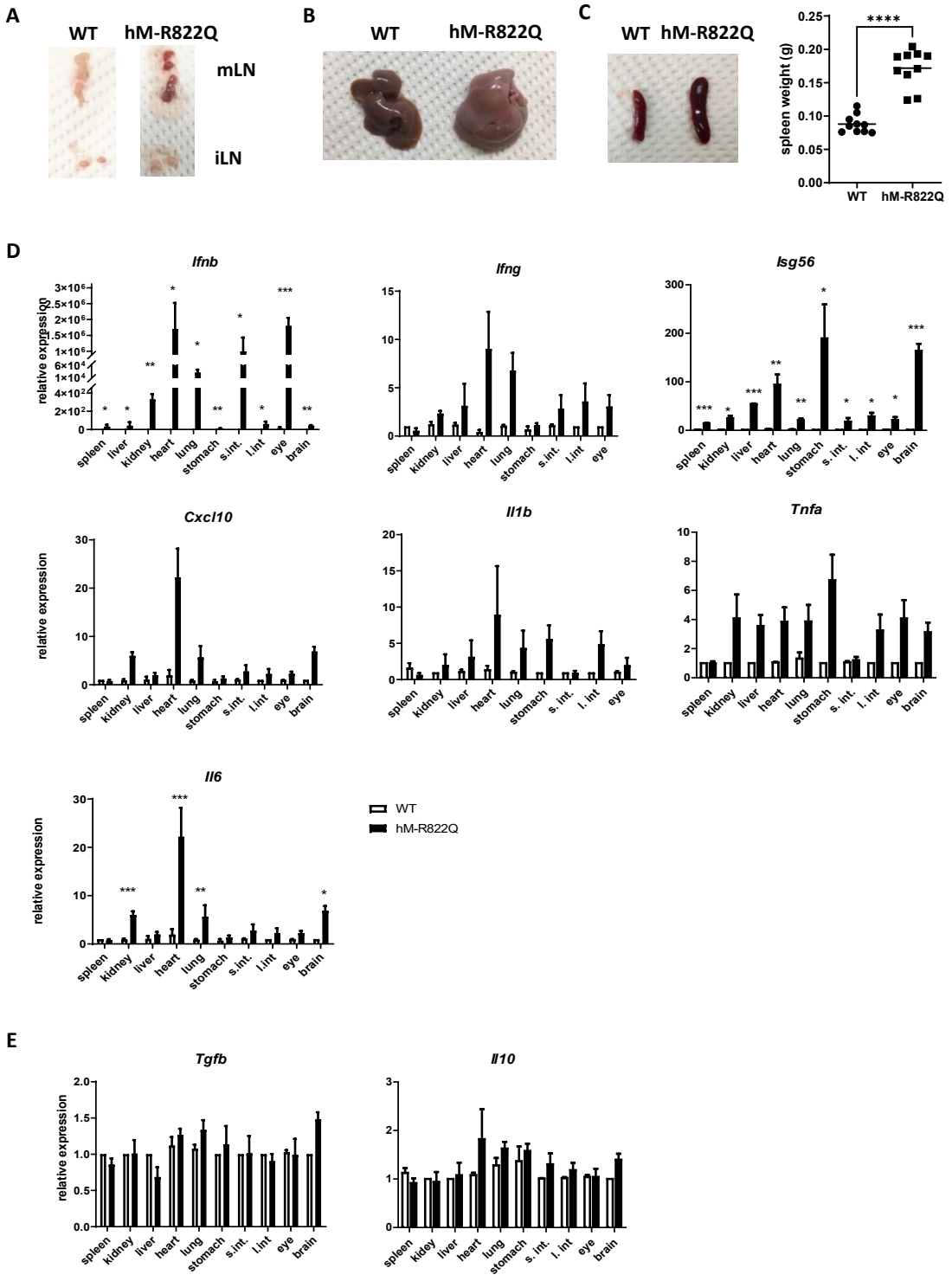

Figure 4. Systemic inflammation. Representative image of WT and hM-R822Q Tg mesenteric lymph nodes (mLN) and inguinal lymph nodes (iLN) (A), and livers (B). (C) Representative images of WT and hM-R822Q Tg spleens and spleen weight (n=10). Organ-specific mRNA expression of inflammatory promotors *Ifnb*, *Ifng*, *Isg56*, *Cxcl10*, *Il1b*, *Tnfa*, and *Il6* (D) and inflammatory regulators *Tgfb* and *Il10* (E). Samples were taken from mice aged 8-10 weeks. Graphs are presented as mean ± SEM. Statistical significance was determined using unpaired Student's *t*-test and one-way ANOVA (*p<0.05, **p<0.01, ***p<0.001)

Despite displaying no significant differences in cell splenic populations of macrophages ($F4/80^+CD11b^+$) and dendritic cells ($CD11c^+$) when compared to WT mice, these cells showed increased expression of CD86 activation markers in hM-R822Q Tg mice (Fig. 5A). Similarly, natural killer cells ($NK1.1^+CD3\varepsilon^-$) had elevated surface expression of CD69, indicating increased activation without showing significant increase in cell populations (Fig. 5B). Lymphocytes displayed activation in hM-R822Q Tg mice in the absence of active infection. CD69 expression was elevated in both T cells ($CD19^+$) and B cells ($CD3\varepsilon^+$) of hM-R822Q Tg mice compared to WT mice (Fig. 5C). There were also lower populations of naïve $CD4^+$ and $CD8^+$ T cells, which is coupled with significantly higher population of effector cells, and a trend for increased populations of memory T cells (Fig. 5D). This indicates a primed adaptive immune response was also significantly activated.

Previous studies on *Ifih1*$^{gs/+}$ mouse model bearing the G821S mutant of mouse MDA5 showed a strong lupus-like nephritis phenotype in the kidneys (4). hM-R822Q Tg mice did not display clear morphological symptoms of glomerulonephritis despite the significant deposition of IgG (Fig.6A) and upregulation of autoantibodies (Fig. 6B) in the sera. Comparison with *Ifih1*$^{gs/+}$ mice showed that hM-R822Q Tg mice had relatively decreased cytokine expression (Fig. 6C), suggesting that a threshold of ISG signature and inflammatory cytokine level is critical for the development of overt disease.

In summation, hM-R822Q Tg mice can be described as having systemic inflammation with mild pathology. Cytokine expression and immune cell activity are indicative of risk for organ damage resulting from inflammation, which, taken together, may contribute to the shortened lifespans of hM-R822Q Tg mice.

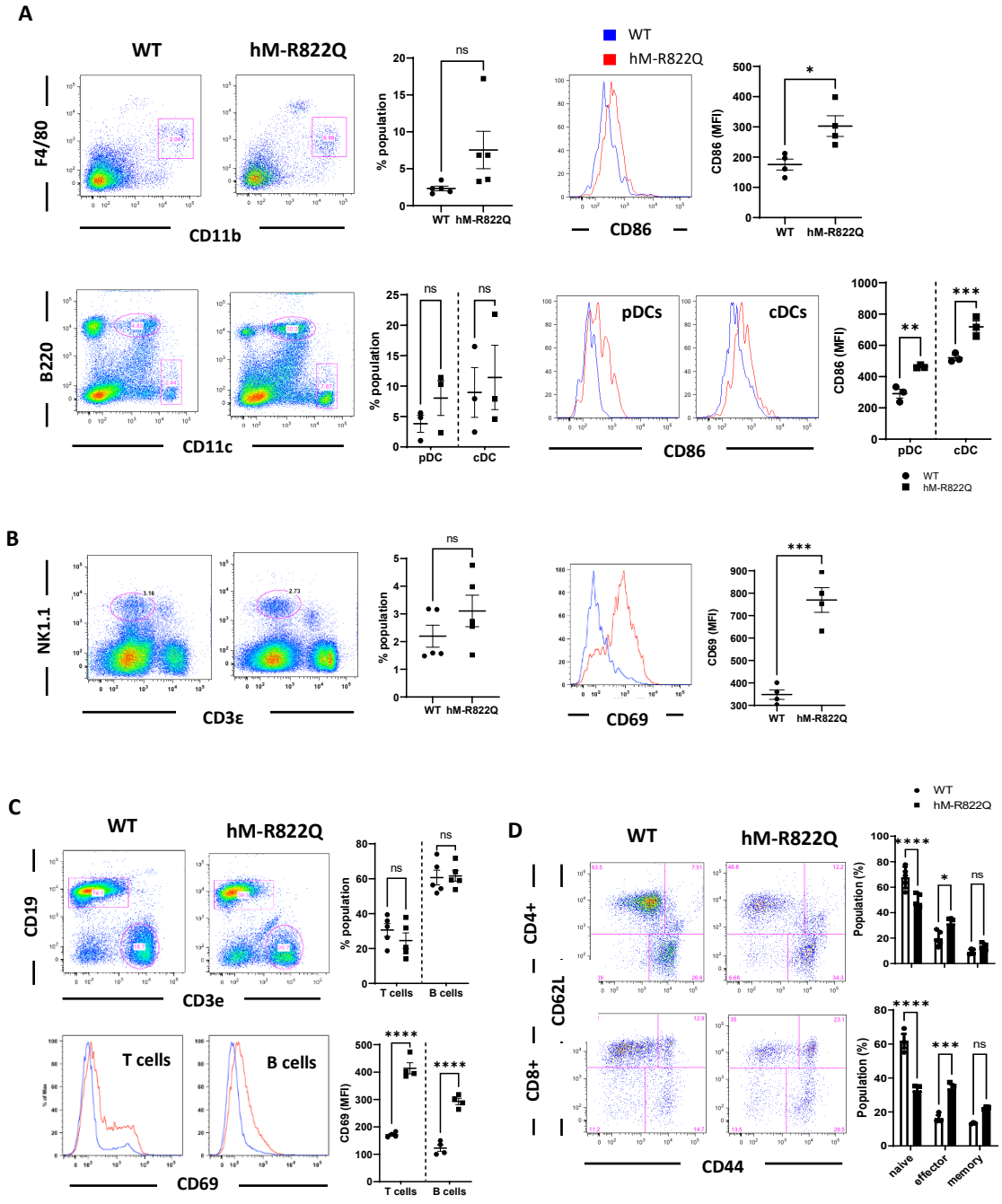

Figure 5. Adaptive and immune cell activation in hM-R822Q Tg mice. Flow cytometry analysis of splenocytes for F4/80^{+}CD11b^{+} macrophage, DC (B220^{+}CD11c^{int} plasmacytoid DCs; B220^{-}CD11c^{hi} conventional DCs) CD86 activation (A), CD69 activation in NK1.1^{+}CD3ε^{-} NK cells (B), T cell (CD19^{+}) and B cell (CD3ε^{+}) activation (C) and CD4^{+} and CD8^{+} T cell activation (D). Flow cytometry data are representative of at least three independent experiments, in mice 10-16 weeks in age, with similar results. Graphs are presented as mean ± SEM. Unpaired Student's *t*-test was used to compare WT and hM-R822Q samples (ns, no statistical significance (p>0.05), *p<0.05, **p<0.01, ***p<0.001, ****p<0.0001).

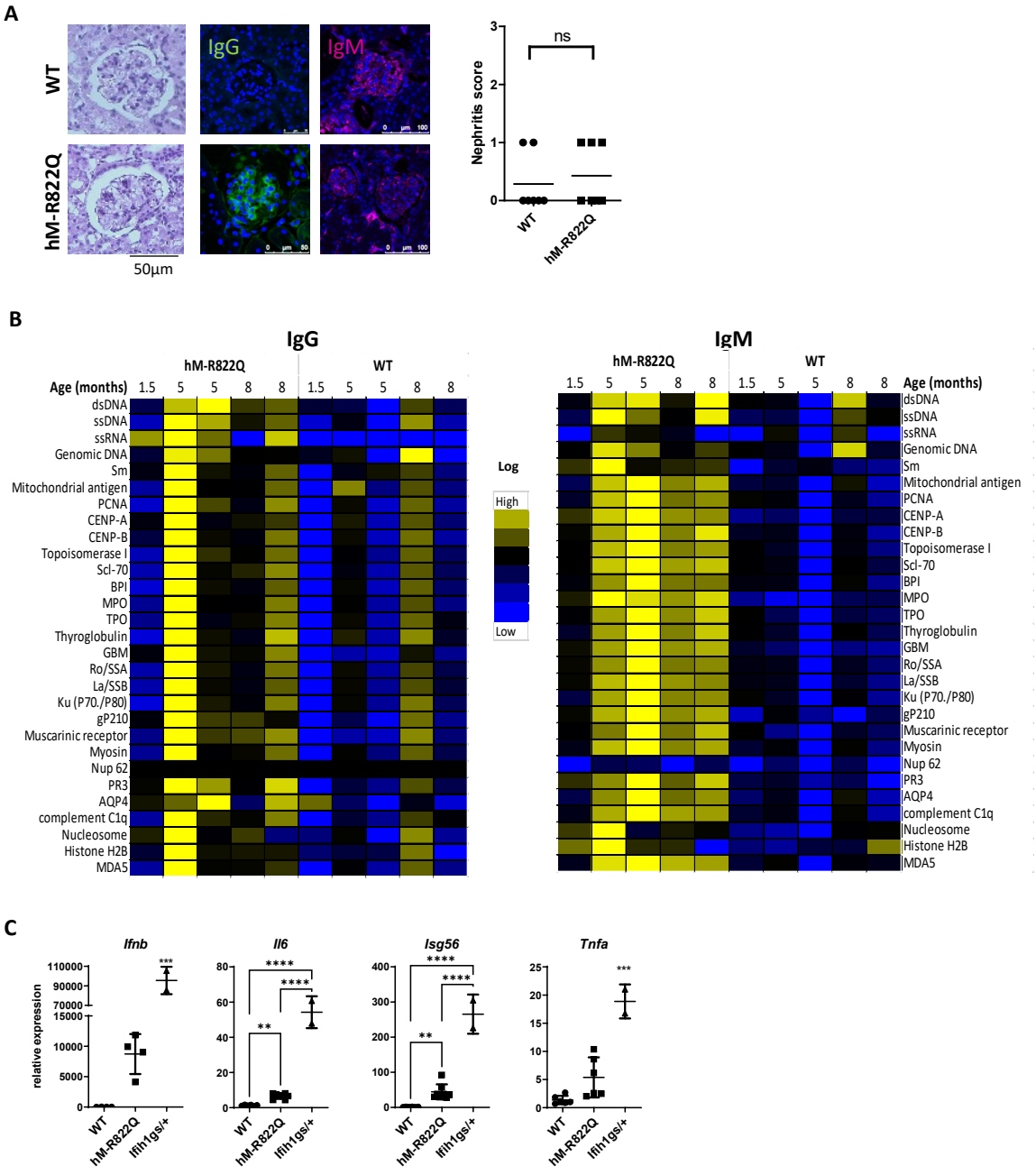

Figure 6. Presence of autoantibodies in hM-R822Q Tg kidneys without nephritis symptoms. (A) Representative image of HE stained section of the glomerulus and immunostaining for IgG and IgM (left). (B) Histology score for the kidney (right). Heat map of autoantibody affinity for IgG and IgM. (C) Kidney mRNA analysis for expression of *Ifnb*, *Il6*, *Isg56*, and *Tnfa* in wild-type (n=6), hM-R822Q transgenic (n=6), and *Ifih1*$^{gs/+}$ mutant (n=2) mice aged 8-10 weeks. Graphs are presented as mean ± SEM. Unpaired Student's *t*-test and one-way ANOVA were used to compare WT and mutant nephritis scores and mRNA expression, respectively (ns, no statistical significance (p>0.05), **p<0.01, ***p<0.001, ****p<0.0001).

3.2 hM-R822Q Tg mice exhibited developmental and bone abnormalities

Body weights were taken as a primary assessment of development and potential chronic or acute irregularities. At 10 weeks hM-R822Q Tg mice showed significantly decreased body weight compared to their WT littermates (Fig. 7A). Body weight kinetics showed this to be consistent throughout the mouse development and aging (Fig. 7B). Together with these signs of growth retardation, hM-R822Q Tg mice showed abnormalities in spine curvature, noticeable from as early as 14 weeks (Fig. 8A). There were no remarkable abnormalities in the bone structure, with hM-R822Q Tg mice showing no observable irregularities in femoral bone (Fig. 8B), nor any significant difference in bone mineral density of hM-R822Q mice (Fig. 8C, 8D) compared to WT mice. Despite this, bone marrow macrophages from hM-R822Q Tg mice induced for osteoclast differentiation with M-CSF and RANKL showed decreased osteoclastogenesis, marked by multinucleated TRAP-positive cell formation (Fig. 8E). This indicated impaired osteoclast differentiation compared to WT mice. These observations are consistent with the development of bone abnormalities observed in patients of SMS.

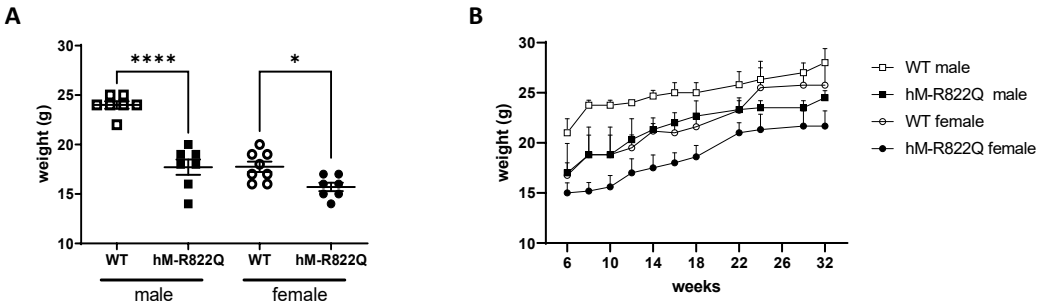

Figure 7. Decreased body weight in hM-R822Q Tg mice. Comparison of body weights (A) at 10 weeks (n=7) and the kinetic of weight gain (B) of WT and hM-R822Q Tg mice (n=10). Results are presented as mean ± SEM. Unpaired Student's *t*-test was used to compare WT and hM-R822Q samples (*p<0.05, ****p<0.0001).

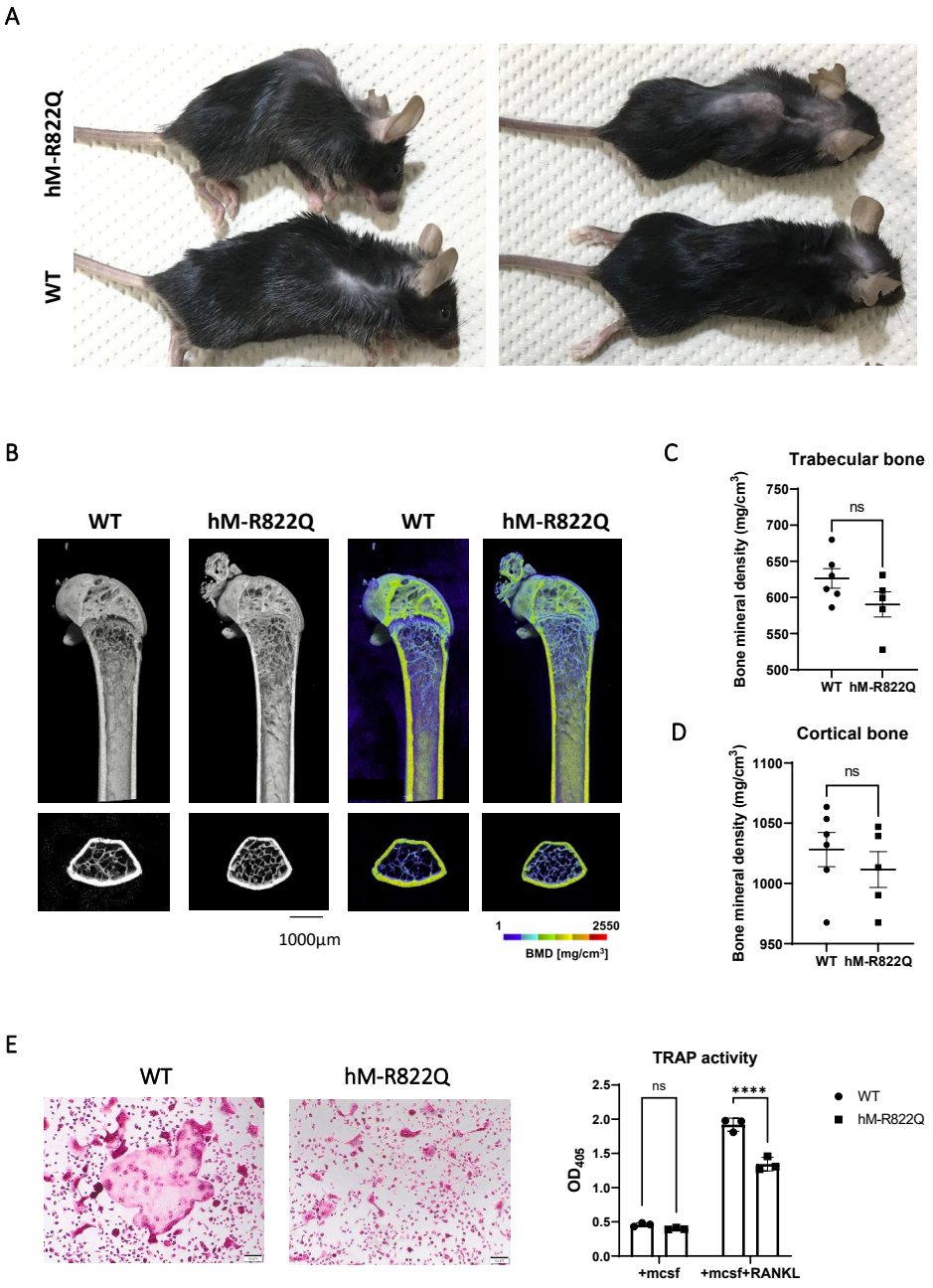

Figure 8. hM-R822Q mice with bone abnormalities. (A) Image of an hM-R822Q Tg mouse demonstrating abnormal spine curvature in contrast to a WT mouse. (B) Representative µCT images (left) and visualization of the bone mineral density of the distal femur (right) from hM-R822Q Tg mice and their wild-type littermates. The bone mineral density in the trabecular bone (C) and cortical bone (D) was measured by µCT analysis (n = 5). (E) In vitro differentiation of osteoclasts from BMMs induced with 10 ng/ml M-CSF and 40 ng/ml of RANKL from wild-type and hM-R822Q Tg mice. Osteoclasts were stained for TRAP (left) and osteoclast formation levels were determined by measuring TRAP activity in cell lysates (n = 3) (right). Mice were analyzed at 10 and 14 weeks. Graphs are presented as mean ± SEM. Unpaired Student's *t*-test was used to compare WT and hM-R822Q samples (ns, no statistical significance ($p>0.05$), *$p<0.05$, **$p<0.01$, ***$p<0.001$, ****$p<0.0001$).

3.3 hM-R822Q Tg mice exhibited SMS-like cardiac pathogenesis

One of the most common causes of early death in SMS patients stems from the development of cardiac and aortic abnormalities (44). Calcification in the aorta and aortic and mitral valves, as well as damage due to the strain of inflammation on the heart, heart valves, and blood vessels, can lead to fatal irregularities in cardiac rhythm (57). Consistent with this, signs of valve degeneration, valve enlargement, and increased levels of cardiac fibrosis were observed in hM-R822Q Tg mice (Fig. 9A). There were also cases of severe leukocyte infiltration seen in BALB/c hM-R822Q Tg mice (Fig. 9B). Immunostaining of the heart structure revealed elevated IgG deposition and alpha-smooth muscle actin (α-SMA) (Fig. 9C), which are markers of calcification and tissue scarring.

A closer look at the underlying heart RNA expression profile revealed activation of IFN-I signaling, with highly upregulated levels of *Ifnb* and *Isg56* (Fig. 9D) in Tg mice. Two of the cytokines known to be increased in cases of calcified aortic valve disease (CAVD), *Il6* and *Tnfa* (58), were also increased in hM-R822Q Tg hearts compared to WT levels. Cytokines known to play more regulatory functions in inflammation such as *Tgfb* and *Il10* showed no difference in expression (Fig. 9E). Similar to the heart, the hM-R822Q Tg aorta showed an IFN-I signature with elevated expression *Ifnb*, *Il6*, *Isg56* and *Tnfa* (Fig. 9F). This corresponded with significantly elevated calcium content in the aortas of hM-R822Q Tg aortas compared to WT mice (Fig. 9G).

Overall, cytokine expression profiles of the heart and aorta display an inflammatory signature that is conducive to calcification. Cell infiltration and antibody deposition also show a propensity for autoimmune damage. Increased levels of aortic calcium, heart fibrosis, and mild valve degeneration showed a strong similarity to SMS-like cardiac calcifications.

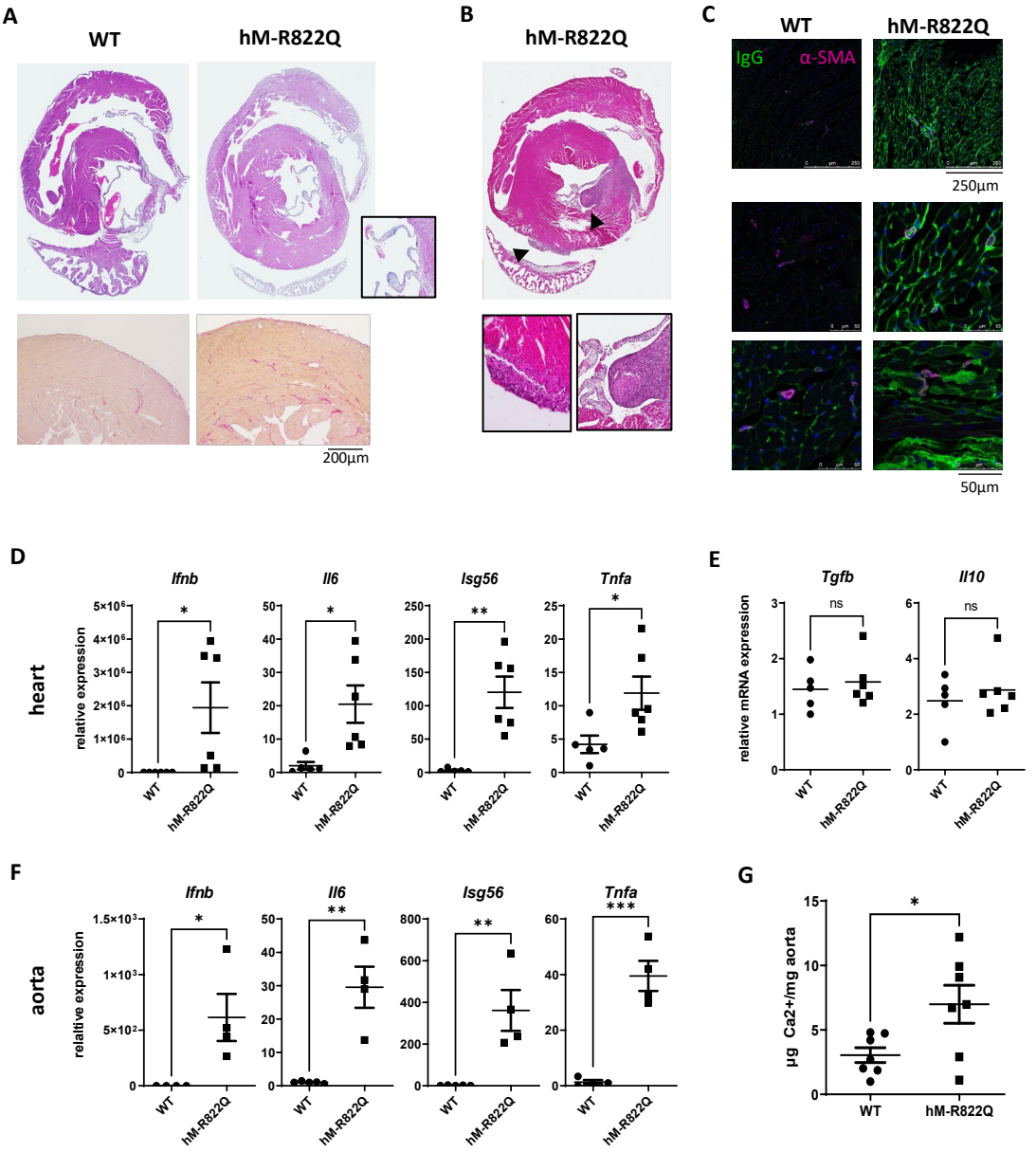

Figure 9. Heart and aortic pathogenesis in hM-R822Q mice. (A) Representative images of HE-stained (above) and picrosirius red-stained (below) heart sections of WT and hM-R822Q mice. Enlarged aortic valves of the hM-R822Q Tg are magnified (inset). (B) HE-stained heart section showing severe leukocyte infiltration (black arrow; magnified below). (C) Immunostaining of IgG and α-SMA on heart sections of WT and hM-R822Q Tg mice. Cytokine mRNA expression of *Ifnb*, *Il6*, *Isg56*, and *Tnfa* (D) and *Tgfb* and *Il10* (E) in the heart (n=6) and *Ifnb*, *Il6*, *Isg56*, and *Tnfa* in the aorta (F) (n=4) relative to *Gapdh*. (G) Ca^{2+} levels measured in the aorta (n=7). Heart and aorta samples were taken from mice aged 8-12 weeks. Results are shown as mean ± SEM analyzed through unpaired Student's *t*-test (ns, no statistical significance (p>0.05), *p<0.05, **p<0.01, ***p<0.001).

3.4 Poly(I:C) induced lethal inflammation in female C57BL/6J hM-R822Q Tg mice

To gain insight into how the symptoms resulting from MDA5 R822Q may be affected by environmental factors and external triggers of immune response, an assessment of what phenotype may be induced in the mutant mice was made using poly(I:C). Poly(I:C), which is a synthetic analog of dsRNA, mimics virus infection by triggering dsRNA sensors. Poly(I:C) treatment introduced through intraperitoneal injection to male hM-R822Q Tg mice did not produce any visible disease phenotype. In contrast, female mice displayed inflammation in the eye region with mucosal discharge (Fig. 10A), and diarrhea within 16 hours post-injection. Marked signs of malaise were observed, resulting in severe weakness and death of 75% of the mice within 22 hours of injection (Fig. 10B). Although both WT and hM-R822Q female mice lost weight following poly(I:C) injection, female hM-R822Q Tg mice lost a significantly higher percentage of weight relative to their weights pre-injection (Fig. 10C).

Consistent with these observations, infection with influenza A virus (IAV) and injection with lipopolysaccharide (LPS) proved to be similarly lethal to hM-R822Q Tg mice. Intranasal inoculation of IAV caused the death of 1 of 4 WT female mice 14 days following inoculation while hM-R822Q Tg mice displayed a 75% mortality (3 of 4 mice) (Fig. 10D). Body weights of these infected mice revealed that IAV infection caused notable weight loss in both WT and hM-R822Q Tg mice (Fig. 10E). Weight loss was significantly lower in WT mice with signs of recovery after 13 days. hM-R822Q Tg mice continued to progress, indicating that inflammation was not resolved. LPS also caused mortality in hM-R822Q Tg mice as early as 17 hours following injection (Fig. 10F).

Diarrhea observed in hM-R822Q Tg mice was an indication of inflammation in the gut. Upon dissection of poly(I:C)-injected mice, there was visible intestinal distension in female hM-R822Q Tg mice that was not observed in either WT or male hM-R822Q Tg mice (Fig. 11A). Histology revealed severe villous shortening, detachment and shedding of the epithelial layer, and cellular infiltration in the small intestine of the poly(I:C)-injected Tg mice. Tg mice also displayed

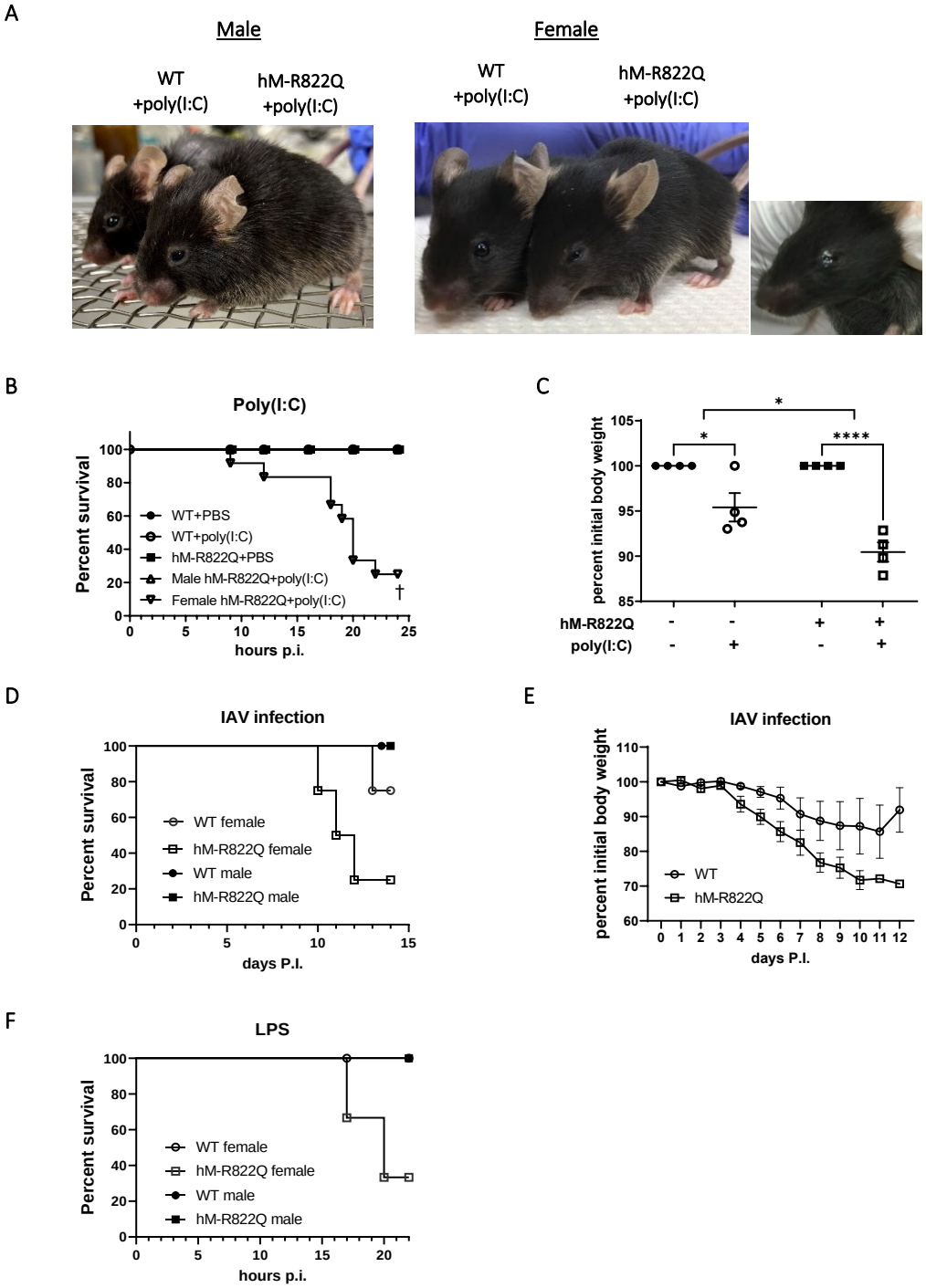

Figure 10. Poly(I:C) induces inflammation and mortality in female hM-R822Q Tg mice. (A) Representative images of male and female WT and hM-R822Q Tg mice 20 hours after poly(I:C) injection. Female hM-R822Q Tg mice accumulate mucosal discharge in the eye region (right). (B) Survival of WT and hM-R822Q Tg mice within 25 hours after *i.p.* injection of 30 ug/g of poly(I:C). (C) Body weights of female mice were measured before injection and 20 hours post-injection, and the percentage based on the initial body weight was calculated (n=4). Survival (D) and body weights (E) of mice was monitored for 14 days after infection with 100 PFU of IAV (n=3). (F) Mouse survival was monitored for 22 hours following *i.p.* injection with 20 µg of LPS (n=3). Survival curves were found significantly different through Kaplan-Meier analysis ($p<0.0001$). Weights are presented as mean ± SEM analyzed using one-way ANOVA (*$p<0.05$, ****$p<0.0001$).

leukocyte infiltration in the large intestine. Meanwhile, poly(I:C)-injected WT mice showed minimal signs of epithelial shedding with no notable cell infiltration (Fig. 11B). In line with these symptoms, gene expression profiles as a result of poly(I:C) injection in hM-R822Q Tg mice were consistent with those observed in inflammatory bowel diseases (IBDs) such as Crohn's disease and ulcerative colitis. Taken as a general marker of cytokine overproduction, *Il6* was upregulated in both the ileum and colon of hM-R822Q mice compared to that in the WT mice (Fig. 11D, 11E). *Il1b* and *Tnfa* mRNA expression were also increased in poly(I:C)-injected hM-R822Q Tg mice. *Il1b* is associated with increased permeability of the intestinal barrier (59, 60) while *Tnfa* is known to be increased in patients of IBD (61, 62). Additionally, splenocytes of poly(I:C)-injected hM-R822Q Tg mice had larger populations of $CD4^+$ cells producing IL-6 (Fig. 11F). IL-6 expression was not limited to the lymphoid organs as significant levels of IL-6 protein were detectable in the serum of female hM-R822Q Tg mice in the basal state, with poly(I:C) injection producing a drastic spike that is not observed in WT mice (Fig. 11G).

To have some understanding of the underlying differences that caused such an extreme gap in the presentation of poly(I:C)-induced symptoms in male and female hM-R822Q Tg mice, it was necessary to investigate what differentiated them not only in the induced but in the basal levels of immune activation. A comparison of *Ifnb* and *Il6* mRNA expression in the ileum revealed that poly(I:C) induced a mild increase in expression in male mice but caused drastic upregulation in female hM-R822Q Tg mice (Fig. 12A). It was noted that Peyer's patches, which are the primary sites of interaction of the immune cells with the gut microflora, could not be detected in the small intestines of female hM-RR822Q Tg mice 20 hours after poly(I:C) injection, despite being present or even enlarged in WT and male hM-R822Q Tg mice. This has been determined as an indicator of immune activation, resulting in B cell egress into the mucosa or even apoptosis (63). This highlighted the significant role played by Peyer's patch cells in the hM-R822Q inflammation. Flow cytometry analysis of cells of the Peyer's patches of the small intestine in the absence of immune induction showed increased populations of Rorγt expressing

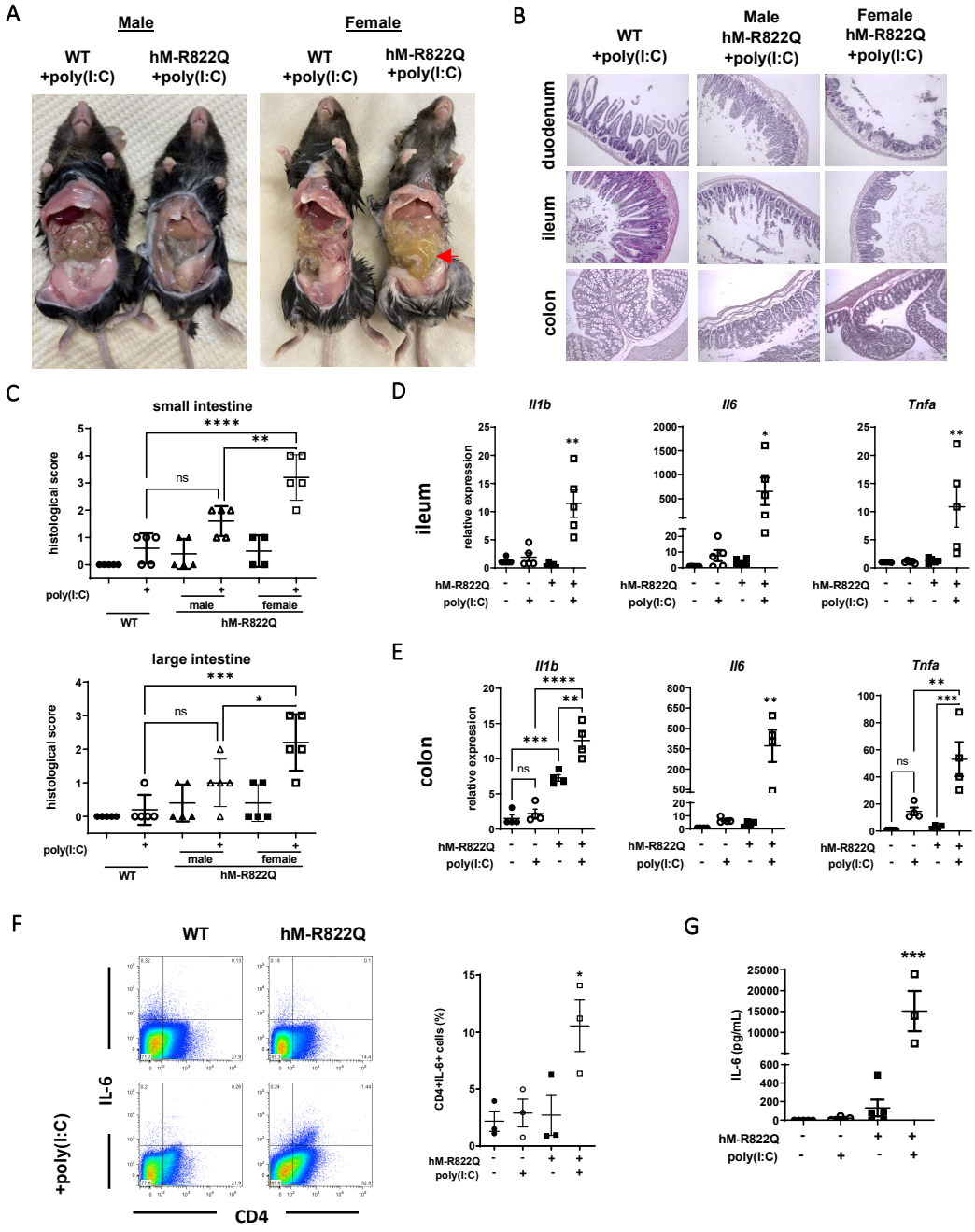

Figure 11. Poly(I:C)-induced intestinal inflammation in female hM-R822Q Tg mice. (A) Images of the abdominal cavity of WT and hM-R822Q Tg mice 20 hours after poly(I:C) injection. Bowel distension (red arrow) is visible in female hM-R822Q Tg. (B) Representative images of HE staining of the small intestines (ileum and duodenum) and colon, sacrificed 20 hours after poly(I:C) injection. (C) Histological scores of WT male and female mice were taken together and segregated for male and female hM-R822Q Tg mice. mRNA expression of *Il1b*, *Il6*, and *Tnfa* in the ileum (D) and colon (E) of female WT and hM-R822Q Tg mice. Flow cytometry analysis of splenocytes for CD4 and IL-6. The data are representative of at least three independent experiments with similar results. (G) IL-6 protein levels detected in the serum of WT and hM-R822Q Tg mice at basal levels (n=5) or following 20 hrs of stimulation with poly(I:C) (n=3). Mice were analyzed at 8-12 weeks of age. Results are shown as mean ± SEM analyzed through one-way ANOVA (ns, no statistical significance (p>0.05), *p<0.05, **p<0.01, ***p<0.001, ****p<0.0001).

cells in hM-R822Q Tg mice (Fig. 12B). However, a corresponding increase in the population of cells expressing the Forkhead box P3 (FoxP3) marker of Tregs was only observed in male hM-R822Q Tg mice. This indicates that, consistent with observations in humans, active immune regulation accompanies the inflammatory immune response in male hM-R822Q Tg mice. In female hM-R822Q Tg mice, Th17 cells remain unchecked, promoting IL-17 expression. This IL-17 expression is observed in the serum of female but not male hM-R822Q Tg mice, when compared with WT mice (Fig. 12D). In addition to the cytotoxic functions of Th17 cells, this functions in the positive feedback of inflammatory cytokines, further inducing the increase in IL-6 expression in female hM-R822Q Tg mice compared to male hM-R822Q Tg mice (Fig. 12E).

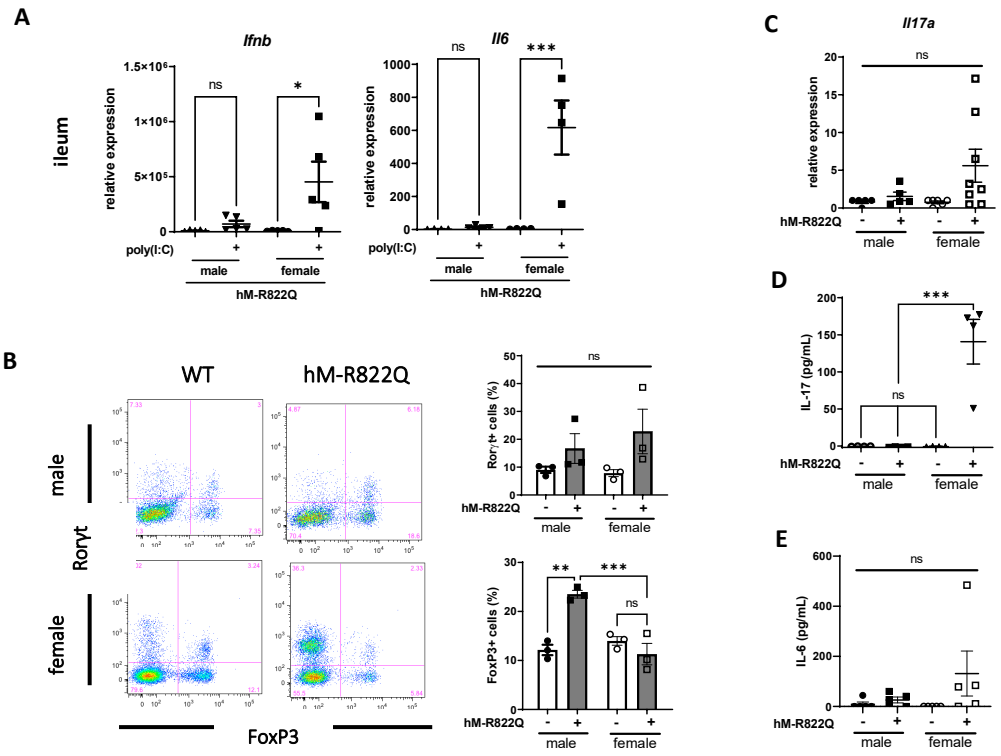

Figure 12. Differential inflammatory signature in male and female hM-R822Q Tg mice. (A) Ileal mRNA expression of *Ifnb* and *Il6* in male and female hM-R822Q Tg mice with and without poly(I:C) injection. (B) Flow cytometry analysis of Peyer's patch $CD4^+$ cells for Rorγt and FoxP3. (C) *Il17a* mRNA levels in the ilea of male and female WT and hM-R822Q Tg mice. (D) IL-17 (n=4) and (E) IL-6 (n=5) in the sera of male and female WT and hM-R822Q Tg mice. Mice were analyzed at 8-12 weeks. Results are shown as mean ± SEM analyzed through unpaired Student's *t*-test and one-way ANOVA (ns, no statistical significance ($p>0.05$), *$p<0.05$, **$p<0.01$, ***$p<0.001$).

In line with observations in several autoimmune diseases and cases of infection, high circulating IL-6 levels were congruent with the development of severe, lethal inflammation characteristic of cytokine storm. One of the hallmarks of cytokine storm syndrome is the occurrence of damage to non-lymphoid or secondary organs. hM-R822Q Tg livers had signs of fibrosis (Fig. 13A). Following poly(I:C) injection, leukocyte infiltration was detectable in hM-R822Q Tg mice. Moreover, cytokine mRNA expression analysis in the liver showed clear upregulation, particularly of *Ifnb*, *Il6*, and *Il1b* (Fig. 13B). hM-R822Q Tg mice showed baseline *Tnfa* upregulation but showed strongly elevated expression in both WT and hM-R822Q Tg livers from poly(I:C) injection.

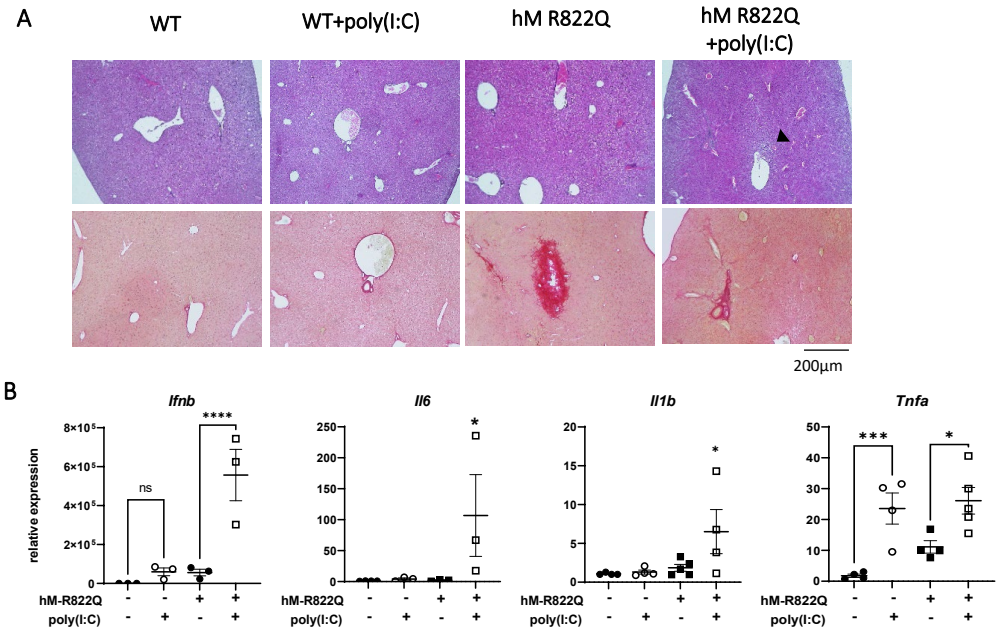

Figure 13. Liver as a target for secondary organ damage in hypercytokinemia. (A) HE staining (above) and picrosirius red staining of the liver, with leukocyte infiltration (black arrow). (B) Liver mRNA transcription levels for *Ifnb*, *Il6*, *Il1b*, and *Tnfa*. Liver samples were taken from mice aged 8-12 weeks (n=4). Graphs are presented as mean ± SEM analyzed using one-way ANOVA (ns, no statistical significance (p>0.05), *p<0.05, ***p<0.001, ****p<0.0001).

Collectively, these findings demonstrate that injection with the MDA5 activator poly(I:C) caused severe inflammation in female hM-R822Q Tg mice. In these mice, the combination of hypercytokinemia and inflammation-induced damage to the mucosa and secondary organs lead to rapid and systemic dysfunction that often resulted in death within the first 24 hours. Despite

the presence of the same mutant transgene, male hM-R822Q Tg mice show evidence of immune regulation, preventing cytokine storm-associated lethality.

3.5 hM-R822Q Tg response to poly(I:C) is determined by background

Similar to C57BL/6J hM-R822Q Tg mice, BALB/c hM-R822Q Tg mice experienced eye inflammation and diarrhea with poly(I:C) injection (Fig. 14A). Notably, however, BALB/c hM-R822Q mice did not exhibit lethality or any sex-specific differences in pathology. Mice exhibited malaise for 24-48 hours, after which they appear to be physically recovered, and are able to survive multiple weekly injections with poly(I:C). This survival despite the appearance of pathological symptoms allowed for a closer observation of the eye inflammation resulting from poly(I:C) injection. Optic nerve tomography revealed some posterior vitreous detachment (Fig.14B) indicative of shrinkage due to fluid extrusion from the vitreous gel, which may result from inflammation (64). Injection of poly(I:C) induced the appearance of tortuous vessels and narrowing of the arteries in hM-R822Q Tg mice, which was not observed in WT mice (Fig. 14C). Similar to C57BL/6J mice, BALB/c hM-R822Q Tg mice showed inflammation-induced damage to the intestinal lining, with notable shedding of cells epithelial layer (Fig. 14D). mRNA expression analysis showed that hM-R822Q mice had elevated levels of *Ifnb*, *Il6*, and *Il1b* (Fig 14E). The ileum showed similar inflammatory signature, with similar upregulation of *Ifnb*, *Il6*, and *Tnfa* between male and female hM-R822Q Tg mice (Fig. 14F). With these observations, it became more puzzling why BALB/c hM-R822Q mice survived despite showing similar signs of inflammation. Some indication was found in the sera where IL-6 levels of BALB/c WT and hM-R822Q Tg mice were below detectable levels. A comparison of the *Ifnb* and *Il6* mRNA expression in the intestines of poly(I:C)-injected mice showed that BALB/c hM-R822Q mice, despite showing elevated cytokine expression compared to WT mice, had drastically reduced levels compared to female C57BL/6J hM-R822Q Tg mice injected with poly(I:C) (Fig. 14G). This indicates that interferon and cytokine levels are determinants of lethality.

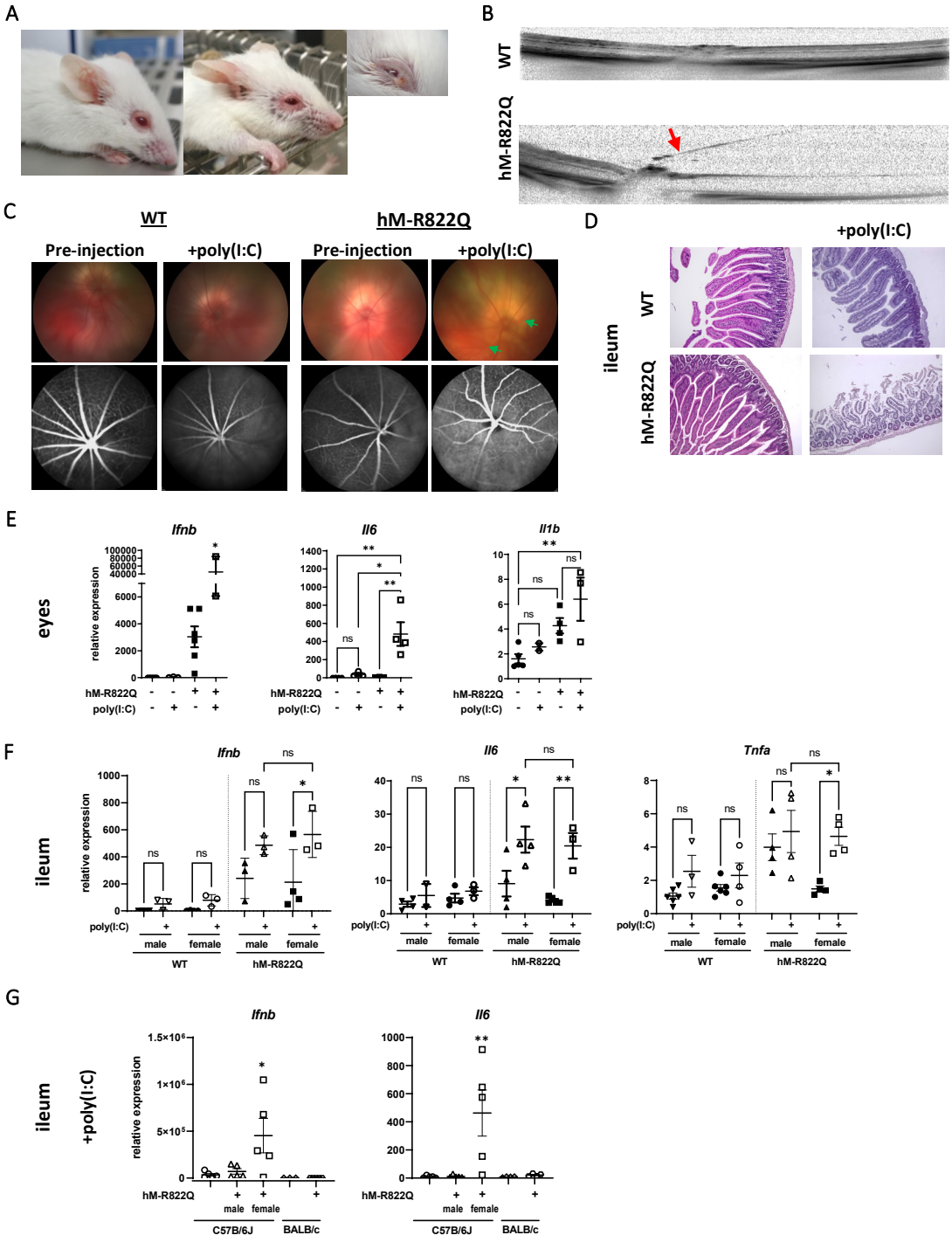

Figure 14. Poly(I:C)-induced inflammation in BALB/c hM-R822Q Tg mice. (A) Representative images of hM-R822Q Tg BALB/c mice displaying inflammation and mucosal discharge in the eyes after poly(I:C) injection. (B) SD-OCT cross-section of poly(I:C)-injected WT and hM-R822Q Tg mice. Red arrow indicates posterior vitreous detachment. (C) Fluorescein angiography of eyes in mice immediately before and 20 hours following poly(I:C) injection. Green arrowheads point to tortuous vessels. Representative HE staining images small intestines (ileum). Eye (E) and ileal (F) mRNA transcription levels of *Ifnb*, *Il6*, and *Tnfa* relative to *Gapdh*. (G) *Ifnb* and *Il6* expression in the ilea of WT and hM-R822Q Tg C57BL/6J and BALB/c mice. Mice were aged 8-12 weeks (n=4). Results are shown as mean ± SEM analyzed through one-way ANOVA (ns, no statistical significance (p>0.05), *p<0.05, **p<0.01).

3.6 MAVS and IFNAR dependent inflammation and poly(I:C) induced pathology

Activation of MDA5 triggers a cascade of inflammatory events that is further amplified by positive feedback mechanism. These pathways involve several key molecules, including MAVS and IFNAR (Fig. 1). MAVS signals directly downstream of RLRs while IFNAR binds to IFN-I, distinguishing whether MDA5 was directly involved in the symptomatology and the importance of IFN signaling in disease outcome. *Mavs*$^{-/-}$ hMDA5 R822Q and *Ifnar1*$^{-/-}$ hMDA5 R822Q mice displayed comparative *Ifnb* mRNA expression to their respective *Mavs*$^{-/-}$ and *Ifnar1*$^{-/-}$ controls (Fig. 15A). In contrast, *Isg56* upregulation was eliminated in *Mavs*$^{-/-}$ hMDA5 R822Q Tg mice but not in *Ifnar1*$^{-/-}$ hMDA5 R822Q mice. This is unsurprising since ISG56 is also induced by IRF3 in an IFN-independent manner (65). Additionally, there was also no notable difference in the lifespans of *Mavs*$^{-/-}$ and *Ifnar1*$^{-/-}$ mice in the presence or absence of the hM-R822Q Tg.

Consistent with the assumption that baseline interferon signature was critical for the development of symptoms due to poly(I:C) injection, female mice in both *Mavs*$^{-/-}$ and *Ifnar1*$^{-/-}$ hM-R822Q showed 100% survival post-injection (Fig. 15B). IL-6 circulation in the serum was also undetectable (Fig. 15C). Sections of poly(I:C) *Mavs*$^{-/-}$ hMDA5 R822Q ileum showed no clear damage in histology, comparable to WT mice. Meanwhile, poly(I:C) induced some villous shortening could be observed in *Ifnar1*$^{-/-}$ hMDA5 R822Q mice, with a significantly reduced histological score compared to hM-R822Q Tg mice (Fig. 15D). This phenotypic reversion could be observed down to the mRNA level in the small intestine, where of *Ifnb*, *Il1b*, and *Tnfa* expression measured at WT levels (Fig. 15E). *Il6* expression in poly(I:C)-injected *Mavs*$^{-/-}$ hMDA5 R822Q mice were reduced 7-fold and in *Ifnar1*$^{-/-}$ hM-R822Q mice reduced 11-fold compared to levels observed in poly(I:C)-injected hM-R822Q Tg mice.

Altogether, the direct function of the MDA5 was confirmed through the importance of its constitutive signaling through MAVS. Signaling downstream of the IFN receptor was also critical for the development of disease phenotype, emphasizing the role of sufficient cytokine production and signal amplification. In the absence of at least one of them th hM-R822Q Tg did not induce

sufficient inflammatory signature and inflammation did not develop despite the administration of poly(I:C).

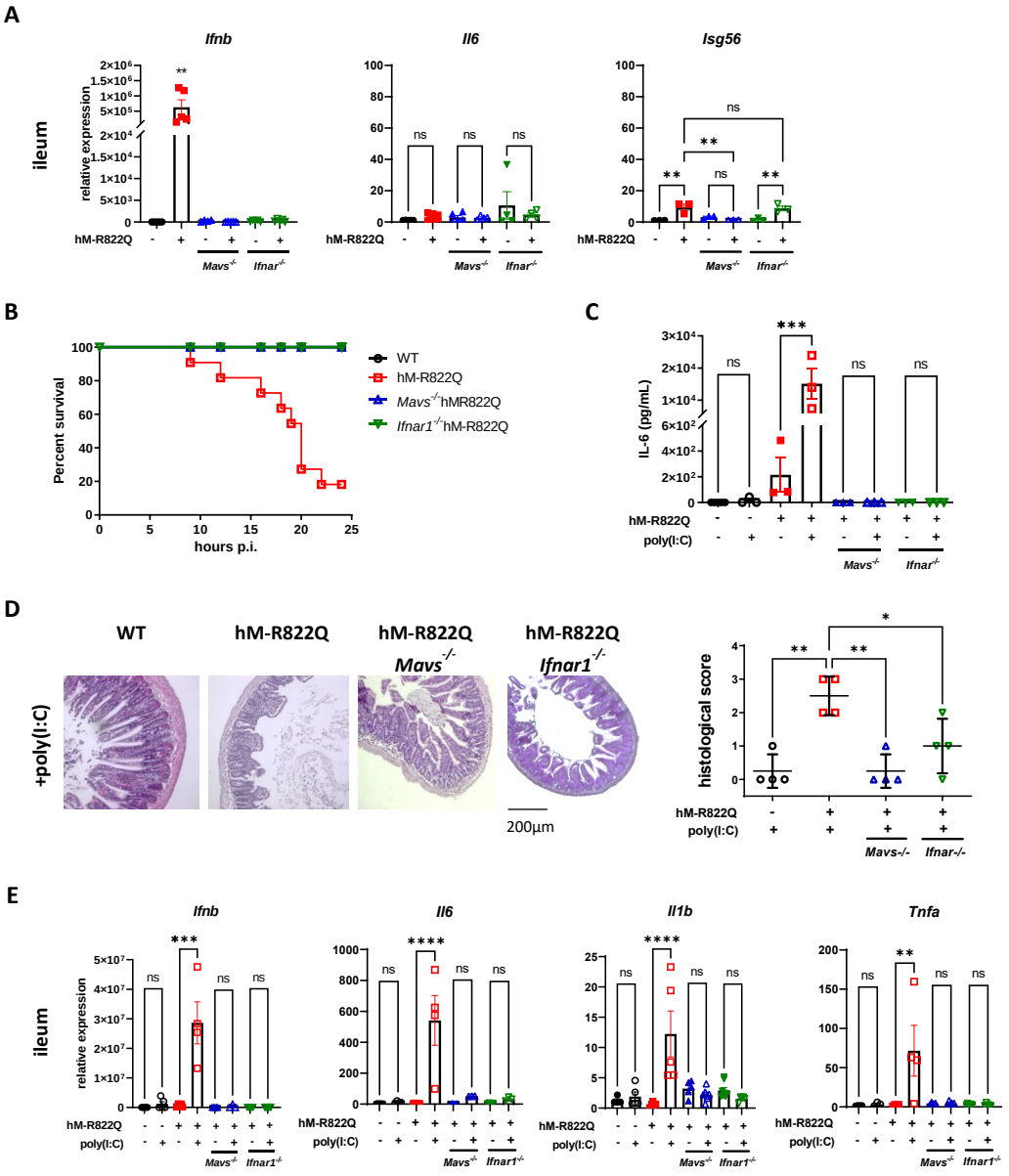

Figure 15. MAVS/IFNAR signaling is critical for poly(I:C)-induced pathogenesis. (A) mRNA expression of *Ifnb*, *Il6*, and *Isg56* in female wild-type, *Mavs*$^{-/-}$, or *Ifnar1*$^{-/-}$ mice with or without the hM-R822Q Tg. (B) Survival of these mice up to 25 hrs post-injection (n=6). (C) Serum levels of IL-6 protein. (n=3) (D) Representative HE stained images of the ileum after treatment with poly(I:C) in female wild-type, hM-R822Q, *Mavs*$^{-/-}$ hM-R822Q, and *Ifnar1*$^{-/-}$ hM-R822Q Tg mice. (E) Induced mRNA expression of *Ifnb*, *Il6*, *Il1b*, and *Tnfa* in the small intestine. mRNA expression was calculated relative to *Gapdh*. Mice were 8-12 weeks old at the time of analysis. Results are shown as mean ± SEM analyzed through unpaired Student's *t*-test and one-way ANOVA (ns, no statistical significance (p>0.05), *p<0.05, **p<0.01, ****p<0.0001).

3.7 JAK signaling is critical for organ damage and lethality of poly(I:C) treatment

JAK/STAT signaling occurs downstream of both the IFN and IL receptors, including IL6R. Mice were treated with tofacitinib, a commercially available JAK inhibitor, as a means not only of confirming the role of these downstream signals in the interferonopathy observed in hM-R822Q Tg mice, but also to test the potential efficacy of drug inhibition to negate the inflammatory signal. Following the diagram shown in Fig. 16A, mice were given daily oral gavage of tofacitinib or vehicle control for 4 days. On the 4th day, poly(I:C) was injected after the gavage. Injection of poly(I:C) to hM-R822Q Tg mice treated only with vehicle control died in the 48 hours following injection (Fig. 16B). This lethality was not observed in hM-R822Q Tg mice treated with tofacitinib, where 100% of survival was observed in the mice tested. Observations were similar in both vehicle and tofacitinib-treated WT mice. To assess the impact of the treatment on poly(I:C)-induced hypercytokinemia, sera taken 20 hours after poly(I:C) injection were analyzed for IL-6 protein. Although, following poly(I:C) injection, IL-6 was detectable in the serum of tofacitinib-treated hM-R822Q Tg mice, compared to Tg mice treated with vehicle control, they exhibited 6-fold reduction (Fig. 16C). Correspondingly, tofacitinib-treated hM-R822Q mice did not display bowel distension following poly(I:C) injection (Fig. 16D). The ileum also did not show significant signs of villous lifting or epithelial shedding (Fig. 16E). Consist with this reduced inflammation, mRNA expression in the small intestine of hM-R822Q Tg mice displayed lower transcript levels of *Ifnb*, *Il6*, and *Il1b* when they were treated with tofacitinib before poly(I:C) injection (Fig. 16F). Furthermore, JAK inhibition was also able to reduce the poly(I:C)-induced inflammatory gene expression in non-mucosal organs such as the liver (Fig. 16G).

On the whole, these data confirm that the blockade of JAK signaling can effectively reduce the hyper-responsiveness in hM-R822Q Tg mice, rescuing mice from lethal inflammation. Damage at the organ level was reduced, and cytokine storm-like symptoms were abrogated.

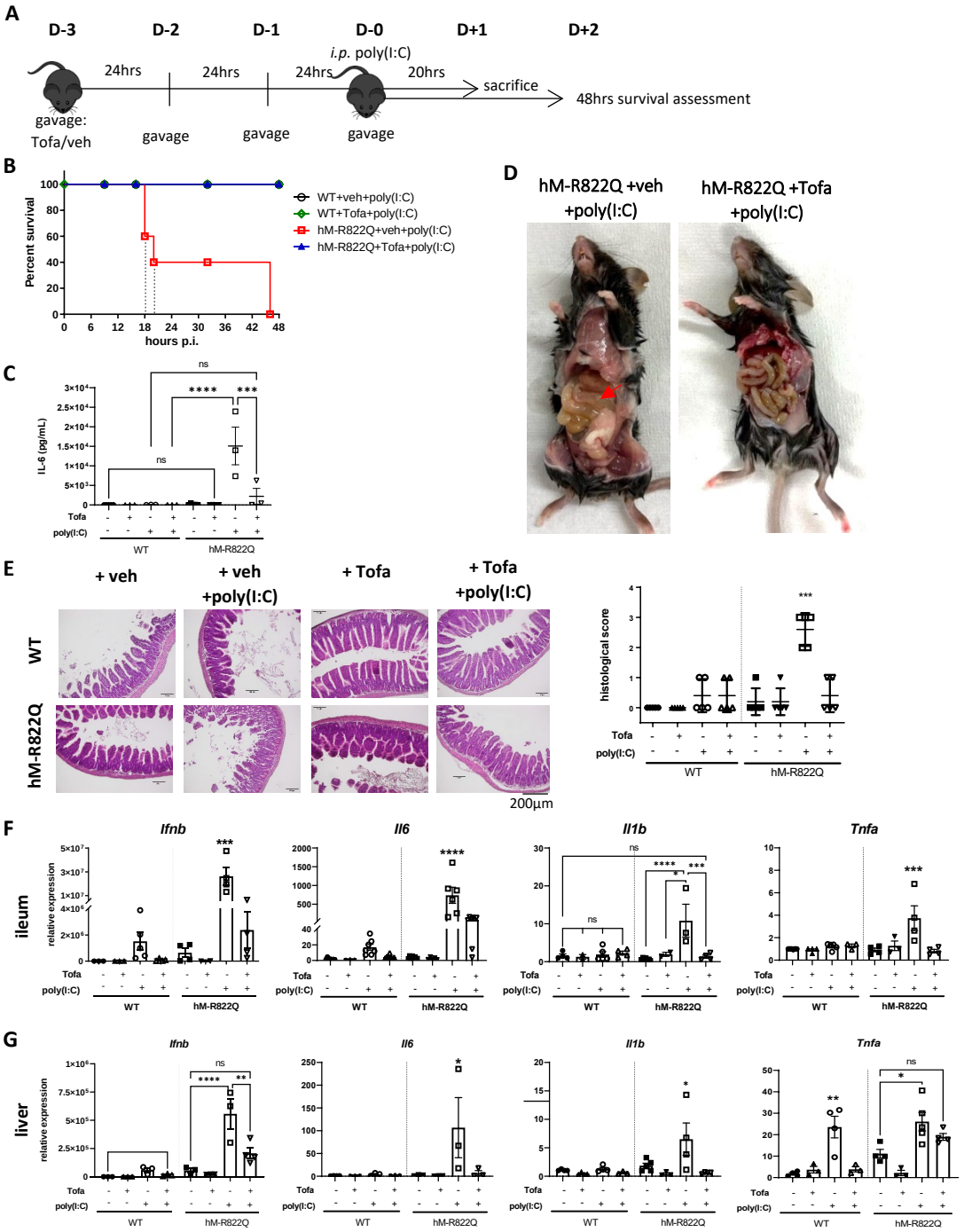

Figure 16. Inhibition of Jak signaling reduces poly(I:C)-induced inflammatory phenotype. (A) Schematic of mouse treatment displaying daily gavage of 600 µg of tofacitinib (Tofa) or vehicle for 3 days (D-3 to D-1). Intraperitoneal injection of 300 µg of poly(I:C) and gavage are concurrently given on D-0, 20 hours before mouse sacrifice for analyzed mice (D+1). (B) Survival assessment of wild-type and hM-R822Q Tg littermates (n=3) within 48 hours following treatment. (C) IL-6 protein levels in the serum analyzed by ELISA. (D) Images of the abdominal cavity of hM-R822Q Tg mice injected with poly(I:C) following 4 days of gavage of vehicle or tofacitinib. (E) Representative HE-staining of the ileum for WT and hM-R822Q Tg mice with and without poly(I:C) injection, treated with vehicle or tofacitinib. *Ifnb*, *Il6*, *Il1b*, and *Tnfa* mRNA expression in the ileum (F) and liver (G) (n=4). Treatments were performed on mice aged 8-12 weeks. Results are shown as mean ± SEM analyzed through unpaired Student's *t*-test and one-way ANOVA (ns, no statistical significance (p>0.05), *p<0.05, **p<0.01, ***p<0.001, ****p<0.0001).

Chapter 4

DISCUSSION

Gain-of-function mutation in positive regulators of IFN signaling is one of the most common mechanisms of interferonopathies (19). The R822Q mutation of MDA5, which is believed to affect the stability of MDA5 nteraction with dsRNA, results in constitutive activation of MDA5. This leads to an elevated basal interferon signature even in the absence of active infection. The lack of overt disease in hM-R822Q mice for at least the first year indicates that a threshold of interferon and cytokine level must be superseded for pathology to develop. Indeed, this is supported by the comparison of pro-inflammatory cytokine expression between hM-R822Q mice and the more severe *Ifih1*$^{gs/+}$ mouse model. Although the R822Q mutation on human MDA5 and the G821S mutation on the *Ifih1*$^{gs/+}$ mice are sequentially adjacent, factors such as the presence of 2 copies of WT mouse *Ifih1*, as well as the functional compatibility of the transgenic human MDA5 in the mouse system may have affected the downstream activity of MDA5 signaling. As a result, the progression of disease appears to be slower and less severe in hM-R822Q Tg mice than in *Ifih1*$^{gs/+}$ mice. This, in turn, makes the development of disease phenotype more tractable and allows the testing of potential treatments.

The R822Q mutation of MDA5 was originally found in patients of SMS who have symptoms including aortic calcification, skeletal and dental abnormalities, and in some cases glaucoma, and recurrent infections. In line with skeletal abnormalities, hM-R822Q Tg mice displayed abnormalities in bone structure and osteoclast development. The inflammatory signature in the mRNA profile, as well as the observed impairment of osteoclast differentiation, demonstrated conditions that are precursory to abnormal tooth eruption and tooth movement (33). The absence of dental abnormalities in hM-R822Q Tg mice may be the effect of the differences in human and mouse dental development (66, 67). Likewise, normal internal eye pressure indicated the absence of glaucoma. However, inflammation in the eye region following poly(I:C) injection indicates the eye as a vulnerable organ in hM-R822Q Tg mice. The heart also showed strong SMS-associated pathogenesis. Although valve enlargement and fibrosis in the heart were only slightly increased, elevated calcification of the aorta indicated a high risk for dysfunction. This predisposition of hM-R822Q Tg mice to vascular pathology was supported by mRNA

expression data. In particular, TNF-α, IL-1β, and IL-6 upregulation were found to have a causative correlation with aortic valve and vascular mineralization (27, 34–38).

One possible consequence of these heart and vascular abnormalities in hM-R822Q Tg mice may be shorter lifespans compared with their WT counterparts. As the hM-R822Q Tg mice aged, skeletal abnormalities, as indicated by vertebral posture, were more prominent in the Tg mice than in WT mice. This leads to the speculation that the chronic inflammatory signature in the heart and vessels also lead to progressive calcification of the aorta and aortic valves, which, coupled with the accumulation of other inflammation-induced organ damage, may contribute to early death in hM-R822Q Tg mice.

A critical point in the findings of this study is the implication of severe and, in some cases, potentially lethal inflammation that occurs following immune stimulation. Recent studies have highlighted the dangers of hyperinflammation in patients of viral infection, where markers of severe disease, such as elevation in serum levels of IL-6, have been identified (15). hM-R822Q Tg mice demonstrate an example of a high-risk model for hypercytokinemia in situations of infection and dsRNA introduction. Interestingly, the effects are not governed solely by the presence of the mutation, but by a combination of gender and genetic background. While female C57BL/6J hM-R822Q Tg mice suffer lethal inflammation following poly(I:C) injection, both male and female BALB/c hM-R822Q Tg mice suffer non-lethal inflammation, while male C57BL/6J hM-R822Q Tg mice were seemingly asymptomatic, having displayed cytokine upregulation without signs of malaise. This study gives some evidence of the involvement of Treg function in the progression of inflammation to hypercytokinemia. Meanwhile, various studies have shown that genetic background plays a role in response to infection and susceptibility to autoimmune disease (68–70). C57BL/6 mice mount a more Th1 immune response, with a stronger tendency to produce a Th17 response to parasitic infection, whilst BALB/c mice tend to produce a Th2 response, with a higher susceptibility to Treg suppression (71, 72). C57BL/6J mice have also exhibited more severe lung injury, slower recovery from lung damage, and less effective viral clearance of influenza A/H7N9 virus, with higher levels of IL-6 and IL-1β than infected BALB/c

mice (73). A closer look at these disease-associated mutations in mice across multiple backgrounds may help elucidate some genetic basis for sex differences in the development of autoimmune disorders.

Targeting signaling elements through the knockout of MAVS or IFNAR1 proved to reduce the basal inflammatory signature of hM-R822Q Tg mice. Moreover, the absence of these signaling molecules rescued female hM-R822Q Tg mice from poly(I:C)-induced hyperinflammation. Inhibition of JAK signaling demonstrated a similar capacity to control inflammation to non-lethal levels. Although tofacitinib treatment did not reduce poly(I:C)-induced interferon and IL-6 expression to WT levels, inflammation was remarkably controlled, as evidenced not only by decreased cytokine expression but also the absence of visible bowel distension and inflammation damage in the intestines.

Interest in studying the JAK/STAT pathway grew due to its involvement in the transmission of signals from a plethora of cytokines within the same signaling pathway. JAK signaling could easily be blocked with small synthetic compounds referred to as JAK inhibitors or Jakinibs. These inhibitors vary in selectivity, able to target one or several of the identified JAK isoforms (JAK1, JAK2, JAK3, and TYK2). At present, JAK inhibitors are being tested as a treatment for various autoimmune diseases such as systemic sclerosis, SLE (74, 75), RA (76), IBD (77), and a variety of dermatological autoimmune conditions (78). The use of JAK inhibitors as a therapeutic treatment for cases of cytokine storm, particularly during acute infection. Baricitinib and tofacitinib, both non-selective JAK inhibitors, have been approved as emergency treatment in cases of severe acute respiratory syndrome coronavirus 2 (SARS-CoV-2) (79, 80). Tofacitinib, in particular, is a JAK1/2/3 inhibitor approved for use against RA, psoriatic arthritis, ulcerative colitis, and polyarticular course juvenile idiopathic arthritis (80). In this research, treatment with tofacitinib was short-term and served as a means of managing severe acute inflammation. Previous study on SMS-associated hRIG-I E373A Tg mice with skin lesions showed that long-term treatment with tofacitinib showed prophylactic and therapeutic effects on the skin condition (52). Recently, a study by Broser et al. (81) made use of ruxolitinib, a JAK1/2

inhibitor blocking signaling at IFNAR, to treat a young SMS patient with the R822Q MDA5 mutation. Treatment resulted in the improvement of psoriatic skin lesions and muscular dysfunction, and a marked reduction of the interferon signature in the blood. These, together with the current study, validate JAK inhibitor treatment as a promising means of improving SMS prognosis and preventing hyperinflammation-induced complications such as the development of cytokine storm due to infection.

As treatment with JAK inhibitors is more widely applied, risks of side-effects have emerged, including adverse cardiovascular events (82, 83) and increased infection due to non-specific immunosuppression (84). In contrast to having mice with mutated mouse MDA5, hM-R822Q Tg mice possess and therefore express the mutant human MDA5. This difference allows the possibility of testing treatments such as molecular inhibitors that can specifically target human MDA5, allowing more precise immune suppression with a lower risk of compromising the body's ability to combat infection and an increased chance of being translatable to human patients.

To conclude, this study was able to demonstrate that hM-R822Q Tg mice may be effectively used as a model for the development of SMS-associated disease, including heart and aortic calcifications. They show an equally important potential to demonstrate the impact of genetic background as well as environmental factors on affected individuals. Of particular concern as of late are the differential effects of virus infection and even vaccine administration that are seemingly unpredictable. Furthermore, hM-R822Q Tg mice can serve as a tool for establishing both broad and R822Q MDA5-specific treatment strategies.

Chapter 5

REFERENCES

1. Yoneyama, M., M. Kikuchi, T. Natsukawa, N. Shinobu, T. Imaizumi, M. Miyagishi, K. Taira, S. Akira, and T. Fujita. 2004. The RNA helicase RIG-I has an essential function in double-stranded RNA-induced innate antiviral responses. *Nat Immunol* 5: 730–737.

2. Kawai, T., K. Takahashi, S. Sato, C. Coban, H. Kumar, H. Kato, K. J. Ishii, O. Takeuchi, and S. Akira. 2005. IPS-1, an adaptor triggering RIG-I- and Mda5-mediated type I interferon induction. *Nat Immunol* 6: 981–988.

3. Loo, Y.-M., and M. Gale. 2011. Immune signaling by RIG-I-like receptors. *Immunity* 34: 680–692.

4. Yang, E., and M. M. H. Li. 2020. All About the RNA: Interferon-Stimulated Genes That Interfere With Viral RNA Processes. *Frontiers in Immunology* 11.

5. Schoggins, J. W., and C. M. Rice. 2011. Interferon-stimulated genes and their antiviral effector functions. *Curr Opin Virol* 1: 519–525.

6. Kuka, M., M. De Giovanni, and M. Iannacone. 2019. The role of type I interferons in CD4+ T cell differentiation. *Immunol Lett* 215: 19–23.

7. Seif, F., M. Khoshmirsafa, H. Aazami, M. Mohsenzadegan, G. Sedighi, and M. Bahar. 2017. The role of JAK-STAT signaling pathway and its regulators in the fate of T helper cells. *Cell Communication and Signaling* 15: 23.

8. Brisse, M., and H. Ly. 2019. Comparative Structure and Function Analysis of the RIG-I-Like Receptors: RIG-I and MDA5. *Frontiers in Immunology* 10.

9. Matsumiya, T., and D. M. Stafforini. 2010. Function and Regulation of Retinoic Acid-Inducible Gene-I. *Crit Rev Immunol* 30: 489–513.

10. Lahita, R. G., K. H. Costenbader, R. Bucala, S. Manzi, and M. A. Khamashta. 2021. *Lahita's Systemic Lupus Erythematosus*, 6th ed. Academic Press.

11. Choubey, D., and K. D. Moudgil. 2011. Interferons in Autoimmune and Inflammatory Diseases: Regulation and Roles. *Journal of Interferon & Cytokine Research* 31: 857.

12. Fajgenbaum, D. C., and C. H. June. 2020. Cytokine Storm. *N Engl J Med* 383: 2255–2273.

13. Leser, H. G., V. Gross, C. Scheibenbogen, A. Heinisch, R. Salm, M. Lausen, K. Rückauer, R. Andreesen, E. H. Farthmann, and J. Schölmerich. 1991. Elevation of serum interleukin-6 concentration precedes acute-phase response and reflects severity in acute pancreatitis. *Gastroenterology* 101: 782–785.

14. Nishimoto, N., K. Terao, T. Mima, H. Nakahara, N. Takagi, and T. Kakehi. 2008. Mechanisms and pathologic significances in increase in serum interleukin-6 (IL-6) and soluble IL-6 receptor after administration of an anti–IL-6 receptor antibody, tocilizumab, in patients with rheumatoid arthritis and Castleman disease. *Blood* 112: 3959–3964.

15. Jafrin, S., Md. A. Aziz, and M. S. Islam. 2022. Elevated Levels of Pleiotropic Interleukin-6 (IL-6) and Interleukin-10 (IL-10) are Critically Involved With the Severity and Mortality of COVID-19: An Updated Longitudinal Meta-Analysis and Systematic Review on 147 Studies. *BiomarkerInsights* 17: 11772719221106600.

16. Barrett, D. 2019. IL-6 Blockade in Cytokine Storm Syndromes. In *Cytokine Storm Syndrome* R. Q. Cron, and E. M. Behrens, eds. Springer International Publishing, Cham. 561–568.

17. Huarte, E., M. T. Peel, K. Verbist, B. L. Fay, R. Bassett, S. Albeituni, K. E. Nichols, and P. A. Smith. 2021. Ruxolitinib, a JAK1/2 Inhibitor, Ameliorates Cytokine Storm in Experimental Models of Hyperinflammation Syndrome. *Front. Pharmacol.* 12: 650295.

18. Ioannou, Y., and D. A. Isenberg. 2000. Current evidence for the induction of autoimmune rheumatic manifestations by cytokine therapy. *Arthritis & Rheumatism* 43: 1431–1442.

19. Crow, Y. J., and N. Manel. 2015. Aicardi–Goutières syndrome and the type I interferonopathies. *Nat Rev Immunol* 15: 429–440.

20. Psarras, A., P. Emery, and E. M. Vital. 2017. Type I interferon–mediated autoimmune diseases: pathogenesis, diagnosis and targeted therapy. *Rheumatology* 56: 1662–1675.

21. Pestal, K., C. C. Funk, J. M. Snyder, N. D. Price, P. M. Treuting, and D. B. Stetson. 2015. Isoforms of RNA-Editing Enzyme ADAR1 Independently Control Nucleic Acid Sensor MDA5-Driven Autoimmunity and Multi-organ Development. *Immunity* 43: 933–944.

22. d'Angelo, D. M., P. Di Filippo, L. Breda, and F. Chiarelli. 2021. Type I Interferonopathies in Children: An Overview. *Front Pediatr* 9: 631329.

23. Varzari, A., K. Bruch, I. V. Deyneko, A. Chan, J. T. Epplen, and S. Hoffjan. 2014. Analysis of polymorphisms in RIG-I-like receptor genes in German multiple sclerosis patients. *Journal of Neuroimmunology* 277: 140–144.

24. Lincez, P. J., I. Shanina, and M. S. Horwitz. 2015. Reduced Expression of the MDA5 Gene *IFIH1* Prevents Autoimmune Diabetes. *Diabetes* 64: 2184–2193.

25. Sheng, Y., X. Jin, J. Xu, J. Gao, X. Du, D. Duan, B. Li, J. Zhao, W. Zhan, H. Tang, X. Tang, Y. Li, H. Cheng, X. Zuo, J. Mei, F. Zhou, B. Liang, G. Chen, C. Shen, H. Cui, X. Zhang, C. Zhang, W. Wang, X. Zheng, X. Fan, Z. Wang, F. Xiao, Y. Cui, Y. Li, J. Wang, S. Yang, L. Xu, L. Sun, and X. Zhang. 2014. Sequencing-based approach identified three new susceptibility loci for psoriasis. *Nat Commun* 5: 4331.

26. Martínez, A., J. Varadé, J. R. Lamas, M. Fernández-Arquero, J. A. Jover, E. G. de la Concha, B. Fernández-Gutiérrez, and E. Urcelay. 2008. Association of the IFIH1-GCA-KCNH7 chromosomal region with rheumatoid arthritis. *Annals of the Rheumatic Diseases* 67: 137–138.

27. Funabiki, M., H. Kato, Y. Miyachi, H. Toki, H. Motegi, M. Inoue, O. Minowa, A. Yoshida, K. Deguchi, H. Sato, S. Ito, T. Shiroishi, K. Takeyasu, T. Noda, and T. Fujita. 2014. Autoimmune Disorders Associated with Gain of Function of the Intracellular Sensor MDA5. *Immunity* 40: 199–212.

28. Feigenbaum, A., C. Müller, C. Yale, J. Kleinheinz, P. Jezewski, H. G. Kehl, M. MacDougall, F. Rutsch, and R. C. M. Hennekam. 2013. Singleton-Merten syndrome: an autosomal dominant disorder with variable expression. *Am J Med Genet A* 161A: 360–370.

29. Jang, M.-A., E. K. Kim, H. Now, N. T. H. Nguyen, W.-J. Kim, J.-Y. Yoo, J. Lee, Y.-M. Jeong, C.-H. Kim, O.-H. Kim, S. Sohn, S.-H. Nam, Y. Hong, Y. S. Lee, S.-A. Chang, S. Y. Jang, J.-W. Kim, M.-S. Lee, S. Y. Lim, K.-S. Sung, K.-T. Park, B. J. Kim, J.-H. Lee, D.-K. Kim, C. Kee, and C.-S. Ki. 2015. Mutations in DDX58, which encodes RIG-I, cause atypical Singleton-Merten syndrome. *Am J Hum Genet* 96: 266–274.

30. Pettersson, M., B. Bergendal, J. Norderyd, D. Nilsson, B.-M. Anderlid, A. Nordgren, and A. Lindstrand. 2017. Further evidence for specific IFIH1 mutation as a cause of Singleton–Merten syndrome with phenotypic heterogeneity. *American Journal of Medical Genetics Part A* 173: 1396–1399.

31. Someya, S., A. Uchiyama, K. Arai, K. Kon, S. Yamashina, S. Watanabe, and K. Ikejima. 2022. Gender-specific development of experimental autoimmune cholangitis induced by double-stranded RNA. *Biochemical and Biophysical Research Communications* 588: 90–96.

32. van Vollenhoven, R. F. 2009. Sex differences in rheumatoid arthritis: more than meets the eye... *BMC Med* 7: 12.

33. Weckerle, C. E., and T. B. Niewold. 2011. The Unexplained Female Predominance of Systemic Lupus Erythematosus: Clues from Genetic and Cytokine Studies. *Clin Rev Allergy Immunol* 40: 42–49.

34. Fink, A. L., and S. L. Klein. 2018. The evolution of greater humoral immunity in females than males: implications for vaccine efficacy. *Curr Opin Physiol* 6: 16–20.

35. Fischinger, S., C. M. Boudreau, A. L. Butler, H. Streeck, and G. Alter. 2019. Sex differences in vaccine-induced humoral immunity. *Semin Immunopathol* 41: 239–249.

36. Ursin, R. L., S. Dhakal, H. Liu, S. Jayaraman, H.-S. Park, H. R. Powell, M. L. Sherer, K. E. Littlefield, A. L. Fink, Z. Ma, A. L. Mueller, A. P. Chen, K. Seddu, Y. A. Woldetsadik, P. J. Gearhart, H. B. Larman, R. W. Maul, A. Pekosz, and S. L. Klein. 2022. Greater Breadth of Vaccine-Induced Immunity in Females than Males Is Mediated by Increased Antibody Diversity in Germinal Center B Cells. *mBio* 13: e01839-22.

37. Roussou, E., and S. Sultana. 2011. Spondyloarthritis in women: differences in disease onset, clinical presentation, and Bath Ankylosing Spondylitis Disease Activity and Functional indices (BASDAI and BASFI) between men and women with spondyloarthritides. *Clin Rheumatol* 30: 121–127.

38. Lapierre, P., K. Béland, C. Martin, F. Alvarez, and F. Alvarez. 2010. Forkhead box p3+ regulatory T cell underlies male resistance to experimental type 2 autoimmune hepatitis. *Hepatology* 51: 1789–1798.

39. Nie, J., Y. Y. Li, S. G. Zheng, A. Tsun, and B. Li. 2015. FOXP3+ Treg Cells and Gender Bias in Autoimmune Diseases. *Front. Immunol.* 6.

40. Quintero, O. L., M. J. Amador-Patarroyo, G. Montoya-Ortiz, A. Rojas-Villarraga, and J.-M. Anaya. 2012. Autoimmune disease and gender: Plausible mechanisms for the female predominance of autoimmunity. *Journal of Autoimmunity* 38: J109–J119.

41. Klein, S. L., and K. L. Flanagan. 2016. Sex differences in immune responses. *Nat Rev Immunol* 16: 626–638.

42. Singleton, E. B., and D. F. Merten. 1973. An unusual syndrome of widened medullary cavities of the metacarpals and phalanges, aortic calcification and abnormal dentition. *Pediatr Radiol* 1: 2–7.

43. Gay, B. B., and J. P. Kuhn. 1976. A syndrome of widened medullary cavities of bone, aortic calcification, abnormal dentition, and muscular weakness (the Singleton-Merten syndrome). *Radiology* 118: 389–395.

44. Rutsch, F., M. MacDougall, C. Lu, I. Buers, O. Mamaeva, Y. Nitschke, G. I. Rice, H. Erlandsen, H. G. Kehl, H. Thiele, P. Nürnberg, W. Höhne, Y. J. Crow, A. Feigenbaum, and R. C. Hennekam. 2015. A Specific IFIH1 Gain-of-Function Mutation Causes Singleton-Merten Syndrome. *The American Journal of Human Genetics* 96: 275–282.

45. Valverde, I., E. Rosenthal, A. Tzifa, P. Desai, A. Bell, K. Pushparajah, S. Qureshi, P. Beerbaum, and J. Simpson. 2010. Singleton-Merten Syndrome and Impaired Cardiac Function. *Journal of the American College of Cardiology* 56: 1760–1760.

46. Lässig, C., K. Lammens, J. L. Gorenflos López, S. Michalski, O. Fettscher, and K.-P. Hopfner. 2018. Unified mechanisms for self-RNA recognition by RIG-I Singleton-Merten syndrome variants. *eLife* 7: e38958.

47. Lu, C., and M. MacDougall. 2017. RIG-I-Like Receptor Signaling in Singleton-Merten Syndrome. *Front Genet* 8: 118.

48. Bessueille, L., and D. Magne. 2015. Inflammation: a culprit for vascular calcification in atherosclerosis and diabetes. *Cell Mol Life Sci* 72: 2475–2489.

49. Thongchote, K., S. Svasti, J. Teerapornpuntakit, P. Suntornsaratoon, N. Krishnamra, and N. Charoenphandhu. 2015. Bone microstructural defects and osteopenia in hemizygous βIVSII-654 knockin thalassemic mice: sex-dependent changes in bone density and osteoclast function. *American Journal of Physiology-Endocrinology and Metabolism* 309: E936–E948.

50. Soda, N., N. Sakai, H. Kato, M. Takami, and T. Fujita. 2019. Singleton-Merten Syndrome–like Skeletal Abnormalities in Mice with Constitutively Activated MDA5. *J.I.* 203: 1356–1368.

51. Onizawa, H., H. Kato, H. Kimura, T. Kudo, N. Soda, S. Shimizu, M. Funabiki, Y. Yagi, Y. Nakamoto, J. Priller, R. Nishikomori, T. Heike, N. Yan, T. Tsujimura, T. Mimori, and T. Fujita. 2021. Aicardi–Goutières syndrome-like encephalitis in mutant mice with constitutively active MDA5. *International Immunology* 33: 225–240.

52. Abu Tayeh, A., M. Funabiki, S. Shimizu, S. Satoh, L. Sumin, Y. Iwakura, H. Kato, and T. Fujita. 2021. Psoriasis-like skin disorder in transgenic mice expressing a RIG-I Singleton–Merten syndrome variant. *International Immunology* 33: 211–224.

53. Crampton, S. P., J. A. Deane, L. Feigenbaum, and S. Bolland. 2012. *Ifih1* Gene Dose Effect Reveals MDA5-Mediated Chronic Type I IFN Gene Signature, Viral Resistance, and Accelerated Autoimmunity. *J.I.* 188: 1451–1459.

54. Alexopoulou, L., A. C. Holt, R. Medzhitov, and R. A. Flavell. 2001. Recognition of double-stranded RNA and activation of NF-κB by Toll-like receptor 3. *Nature* 413: 732–738.

55. Kurotaki, Y., N. Sakai, T. Miyazaki, M. Hosonuma, Y. Sato, A. Karakawa, M. Chatani, M. Myers, T. Suzawa, T. Negishi-Koga, R. Kamijo, A. Miyazaki, Y. Maruoka, and M. Takami. 2020. Effects of lipid metabolism on mouse incisor dentinogenesis. *Sci Rep* 10: 5102.

56. Hasegawa, T., H. O. Ikeda, N. Nakano, Y. Muraoka, T. Tsuruyama, K. Okamoto-Furuta, H. Kohda, and N. Yoshimura. 2016. Changes in morphology and visual function over time in mouse models of retinal degeneration: an SD-OCT, histology, and electroretinography study. *Jpn J Ophthalmol* 60: 111–125.

57. Abedin, M., Y. Tintut, and L. L. Demer. 2004. Vascular Calcification: Mechanisms and Clinical Ramifications. *ATVB* 24: 1161–1170.

58. Raddatz, M. A., M. S. Madhur, and W. D. Merryman. 2019. Adaptive immune cells in calcific aortic valve disease. *American Journal of Physiology-Heart and Circulatory Physiology* 317: H141–H155.

59. Shouval, D. S., A. Biswas, Y. H. Kang, A. E. Griffith, L. Konnikova, I. D. Mascanfroni, N. S. Redhu, S. M. Frei, M. Field, A. L. Doty, J. D. Goldsmith, A. K. Bhan, A. Loizides, B. Weiss, B. Yerushalmi, T. Yanagi, X. Lui, F. J. Quintana, A. M. Muise, C. Klein, B. H. Horwitz, S. C. Glover, A. Bousvaros, and S. B. Snapper. 2016. Interleukin 1β Mediates Intestinal Inflammation in Mice and Patients With Interleukin 10 Receptor Deficiency. *Gastroenterology* 151: 1100–1104.

60. Mao, L., A. Kitani, W. Strober, and I. J. Fuss. 2018. The Role of NLRP3 and IL-1β in the Pathogenesis of Inflammatory Bowel Disease. *Front. Immunol.* 9: 2566.

61. Mudter, J., and M. F. Neurath. 2007. Il-6 signaling in inflammatory bowel disease: Pathophysiological role and clinical relevance: *Inflammatory Bowel Diseases* 13: 1016–1023.

62. Perše, M., and A. Unkovič. 2019. *The Role of TNF in the Pathogenesis of Inflammatory Bowel Disease*,. IntechOpen.

63. Ogawa, A., T. Tagawa, H. Nishimura, T. Yajima, T. Abe, T. Arai, M. Taniguchi, K. Takeda, S. Akira, Y. Nimura, and Y. Yoshikai. 2006. Toll-like receptors 2 and 4 are differentially involved in Fas dependent apoptosis in Peyer's patch and the liver at an early stage after bile duct ligation in mice. *Gut* 55: 105–113.

64. Hogan, M. J. 1975. Inflammation and its effect on the vitreous. *Trans Ophthalmol Soc U K (1962)* 95: 378–381.

65. Grandvaux, N., M. Servant, B. Tenoever, G. Sen, S. Balachandran, G. Barber, R. Lin, and J. Hiscott. 2002. Transcriptional Profiling of Interferon Regulatory Factor 3 Target Genes: Direct

Involvement in the Regulation of Interferon-Stimulated Genes. *Journal of virology* 76: 5532–9.

66. Yu, T., and O. D. Klein. 2020. Molecular and cellular mechanisms of tooth development, homeostasis and repair. *Development* 147: dev184754.

67. Hermans, F., L. Hemeryck, I. Lambrichts, A. Bronckaers, and H. Vankelecom. 2021. Intertwined Signaling Pathways Governing Tooth Development: A Give-and-Take Between Canonical Wnt and Shh. *Frontiers in Cell and Developmental Biology* 9.

68. Jessen, B., S. Faller, C. D. Krempl, and S. Ehl. 2011. Major Histocompatibility Complex-Dependent Cytotoxic T Lymphocyte Repertoire and Functional Avidity Contribute to Strain-Specific Disease Susceptibility after Murine Respiratory Syncytial Virus Infection. *J Virol* 85: 10135–10143.

69. Rozzo, S. J., T. J. Vyse, C. G. Drake, and B. L. Kotzin. 1996. Effect of genetic background on the contribution of New Zealand Black loci to autoimmune lupus nephritis. *Proc. Natl. Acad. Sci. U.S.A.* 93: 15164–15168.

70. Takeyoshi, M., and T. Inoue. 1992. H-2 Haplotype and Sex-related Differences in IgG Response to Ovalbumin in Mice. *Experimental Animals* 41: 315–319.

71. Chen, X. 2005. BALB/c mice have more CD4+CD25+ T regulatory cells and show greater susceptibility to suppression of their CD4+CD25- responder T cells than C57BL/6 mice. *Journal of Leukocyte Biology* 78: 114–121.

72. Yordanova, I. A., A. Cortés, C. Klotz, A. A. Kühl, M. M. Heimesaat, C. Cantacessi, S. Hartmann, and S. Rausch. 2019. RORγt+ Treg to Th17 ratios correlate with susceptibility to Giardia infection. *Sci Rep* 9: 20328.

73. Zhao, G., C. Liu, Z. Kou, T. Gao, T. Pan, X. Wu, H. Yu, Y. Guo, Y. Zeng, L. Du, S. Jiang, S. Sun, and Y. Zhou. 2014. Differences in the Pathogenicity and Inflammatory Responses Induced by Avian Influenza A/H7N9 Virus Infection in BALB/c and C57BL/6 Mouse Models. *PLoS ONE* 9: e92987.

74. Mok, C. C. 2019. The Jakinibs in systemic lupus erythematosus: progress and prospects. *Expert Opin Investig Drugs* 28: 85–92.

75. Hasni, S. A., S. Gupta, M. Davis, E. Poncio, Y. Temesgen-Oyelakin, P. M. Carlucci, X. Wang, M. Naqi, M. P. Playford, R. R. Goel, X. Li, A. J. Biehl, I. Ochoa-Navas, Z. Manna, Y. Shi, D. Thomas, J. Chen, A. Biancotto, R. Apps, F. Cheung, Y. Kotliarov, A. L. Babyak, H. Zhou, R. Shi, K. Stagliano, W. L. Tsai, L. Vian, N. Gazaniga, V. Giudice, S. Lu, S. R. Brooks, M. MacKay, P. Gregersen, N. N. Mehta, A. T. Remaley, B. Diamond, J. J. O'Shea, M. Gadina, and M. J. Kaplan. 2021. Phase 1 double-blind randomized safety trial of the Janus kinase inhibitor tofacitinib in systemic lupus erythematosus. *Nat Commun* 12: 3391.

76. Bechman, K., S. Subesinghe, S. Norton, F. Atzeni, M. Galli, A. P. Cope, K. L. Winthrop, and J. B. Galloway. 2019. A systematic review and meta-analysis of infection risk with small molecule JAK inhibitors in rheumatoid arthritis. *Rheumatology (Oxford)* 58: 1755–1766.

77. Olivera, P. A., J. S. Lasa, S. Bonovas, S. Danese, and L. Peyrin-Biroulet. 2020. Safety of Janus Kinase Inhibitors in Patients With Inflammatory Bowel Diseases or Other Immune-mediated Diseases: A Systematic Review and Meta-Analysis. *Gastroenterology* 158: 1554-1573.e12.

78. Schwartz, D. M., Y. Kanno, A. Villarino, M. Ward, M. Gadina, and J. J. O'Shea. 2017. JAK inhibition as a therapeutic strategy for immune and inflammatory diseases. *Nat Rev Drug Discov* 16: 843–862.

79. Solimani, F., K. Meier, and K. Ghoreschi. 2021. Janus kinase signaling as risk factor and therapeutic target for severe SARS-CoV-2 infection. *Eur J Immunol* 51: 1071–1075.

80. Spinelli, F. R., F. Meylan, J. J. O'Shea, and M. Gadina. 2021. JAK inhibitors: Ten years after. *European Journal of Immunology* 51: 1615–1627.

81. Broser, P., U. von Mengershausen, K. Heldt, D. Bartholdi, D. Braun, C. Wolf, and M. A. Lee-Kirsch. 2022. Precision treatment of Singleton Merten syndrome with ruxolitinib: a case report. *Pediatric Rheumatology* 20: 24.

82. Winthrop, K. L., and S. B. Cohen. 2022. Oral surveillance and JAK inhibitor safety: the theory of relativity. *Nat Rev Rheumatol* 18: 301–304.

83. Singh, J. A. 2022. Risks and Benefits of Janus Kinase Inhibitors in Rheumatoid Arthritis — Past, Present, and Future. *New England Journal of Medicine* 386: 387–389.

84. Adas, M. A., E. Alveyn, E. Cook, M. Dey, J. B. Galloway, and K. Bechman. The infection risks of JAK inhibition. *Expert Rev Clin Immunol* 18: 253–261.

Chapter 6

ACKNOWLEDGEMENT

First and foremost, I would like to thank Professor Takashi Fujita, who accepted my insistence and allowed me to be a part of his lab. I am truly grateful for his supervision and support through this experience of a lifetime. I would also like to thank Prof. Hiroki Kato for his constant guidance to the end of my Ph.D. It has been a privilege to learn from him. My thanks to Prof. Noda who has been our supervisor these past few years. I also give my sincere gratitude to Prof. James Hejna for giving both scientific and literary insight at the most critical points. I also give me insight at the most critical points. I also give my thanks to Dr. Andres Canela for his support. Thank you also to all my colleagues at Fujita Lab for being there through the ups and downs. To my family, for all their prayers, even though to this day they don't exactly know yet what it is I am working on. And last, but not least, to my husband, who came into the picture when the ride was at its roughest, but somehow helped the boat stay afloat through the storms of grad school and a pandemic to boot.

This study was supported by independent grants from the Japan Science and Technology Agency, from the Ministry of Education, Culture, Sports, Science and Technology of Japan (innovative areas, infection competency, 24115004), Japan Agency for Medical Research and Development under grants JP17ek0109100h0003 and JP18ek0109387h0001, The Kato Memorial Trust for Nambyo Research, and the Japan Society for the Promotion of Science Core to Core Program. It was also funded by the Deutsche Forschungsgemeinschaft (German Research Foundation) under Germany's Excellence Strategy –EXC2151 –390873048 and TRR237, and by the Deutsche Forschungsgemeinschaft (German Research Foundation) Grant No.369799452 –Project number 404459591.

This thesis is based on material contained in the following scholarly paper:

Francine Lianne Emralino, Saya Satoh, Nobuhiro Sakai, Masamichi Takami, Fumihiko Takeuchi, Nan Yan, Frank Rutsch, Takashi Fujita, and Hiroki Kato

Double-stranded RNA induces mortality in an MDA5-mediated type I interferonopathy model

Journal of Immunology, 2022, doi:10.4049/jimmunol.2200367